An Overview of Microphysical Processes in Ice Sheets: Toward Nanoglaciology

Takeo Hondoh

Institute of Low Temperature Science, Hokkaido University, hnd@lowtem.hokudai.ac.jp

Abstract: In recent years, substantial efforts among ice core researchers have been directed toward understanding microphysical processes occurring in ice sheets, because they could affect significantly the paleoclimatic and paleoatmospheric signals recorded in ice cores. For example, a very large fractionation of N_2 and O_2 found in the transition zone from air bubbles to air hydrates was successfully explained in terms of molecular diffusion in ice [1-4]. More recently, we found very many water-soluble microparticles, of which distributions and behavior must be a key to understand the chemical processes in ice sheets [5-9]. In the present paper behaviors of gas molecules and chemical species in ice sheets are summarized and discussed in the light of recent studies.

Moreover, the anisotropic deformation of ice crystals is taken into consideration in recent research on ice sheet flow dynamics [10-13]. Although a very large anisotropy in plasticity of ice was well established in the 1960's by laboratory experiments, almost all ice sheet flow models developed so far have assumed isotropic ice because of difficulty in modeling the anisotropic deformation. As you will see in this volume, this difficulty can be surmounted by the new models [12, 13]. In the present paper, I will discuss the fundamental dislocation processes in ice to better understand why and how ice deforms in different orientations.

In order to emphasize the importance of integration of microphysical processes more closely with macroscopic phenomena, I will propose a new phase of glaciological research, designated as *nanoglaciology*, for further development of the ice core research.

Key words: Dislocation, stacking fault, plasticity of ice, clathrate hydrate, transition zone, eutectic depth, water-soluble microparticle, firn, gas fractionation, ice core, ice sheet, nanoglaciology.

1. Introduction

Fig. 1 schematically illustrates distributions of various inclusions found in ice sheets until now. Air bubbles formed at around the pore-closure depth are gradually compressed as the depth increases, and then they transform into air hydrates in a certain depth range called the transition zone where both air bubbles and air hydrates coexist. There are no air hydrates above the transition zone and no air bubbles below the transition zone, as shown in Fig. 2 [14]. Proper mechanisms for the transition and the gas fractionation associated with the transition are summarized in section 2.

To better understand chemical analyses data of ice cores, it is worthwhile knowing about water-soluble microparticles, which constitute a missing link between atmospheric aerosols and ion concentrations obtained by ion chromatography analyses of melted ice core samples. Ohno discovered the microparticles for the first time when he focused a micro Raman spectrometer on tiny particles included in the Dome Fuji ice core samples. As shown in Fig. 3, he assigned the chemical compound to each particle successfully [5], although later measurements by Sakurai revealed the hydration numbers *n* and species X more precisely [15]. It should be emphasized that most of the chemical trace species are included as solid microparticles, although there have been many arguments on liquid states of the species along grain boundaries [5, 16].

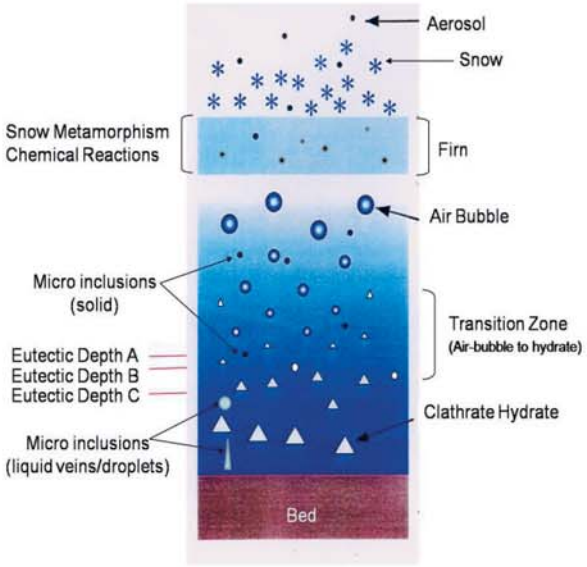

Fig. 1. Various inclusions in ice sheets. Air bubbles transform into clathrate hydrates in the transition zone. Water-soluble microparticles such as Na_2SO_4 transform into the liquid phase below certain eutectic depths where the temperature of ice exceeds the eutectic temperatures of the chemical compounds. Solid, water-insoluble microparticles (dusts or particulates) are included over the whole depth.

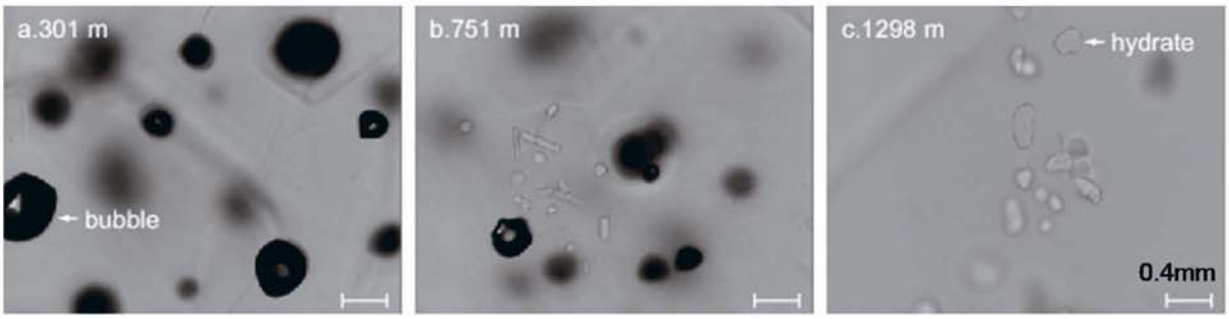

Fig. 2. Characteristic features of air bubbles and clathrate hydrates in the Dome Fuji ice core; the transition zone is from 500 m to 1200 m [14].

However, the solid microparticles must transform into liquid droplets or liquid veins below the eutectic depths depending on the chemical compounds. Since most of the microparticles are salts of sulfate, nitrate and carbonate of which eutectic temperatures are close to the melting temperature of ice, this transformation takes place close to the bed. On the other hand, acids such as H_2SO_4 and some salts such as NaCl have low eutectic temperatures, so that they might exist as a liquid phase in ice even at shallower depths. Therefore, not only concentrations of various ions but also chemical forms of microparticles are important to know as to be described in section 3.

Iizuka carried out SEM-EDS measurements on individual microparticles collected by the sublimation method developed by him [8]. He constructed a new diagram by which major chemical forms of the microparticles can be deduced on the basis of ion chromatography data only [7]. Details of the method and arguments are summarized by Iizuka *et al.* in this volume [17]. Note that water-insoluble microparticles currently designated as dust or particulates are also included as solid microparticles over the whole depth of ice sheets.

In addition to the micro-inclusions stated above, ice also contains lattice defects such as molecular defects (self-interstitials and vacancies), protonic point defects (Bjerrum defects and ionic defects), foreign atoms (molecules) and dislocations. Gas molecules dissolved in ice play an important role in the transformation from air bubbles to clathrate hydrates as to be described in section 2, and self-interstitials play a dominant role in self-diffusion in ice (see subsection 2.3). Electrical properties of ice critically depend on behavior of protonic point defects [18, 19]. Moreover, dislocations play a key role in anisotropic deformation of ice as to be described in section 4.

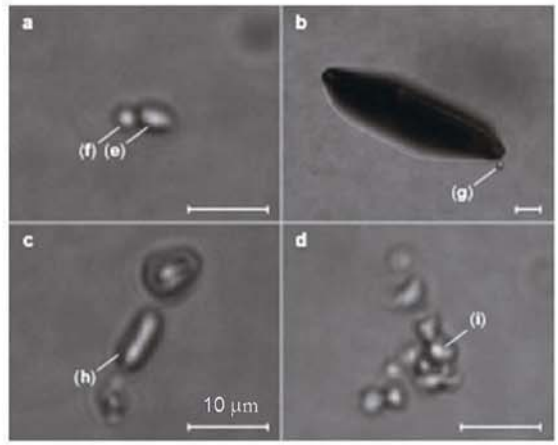

(a)

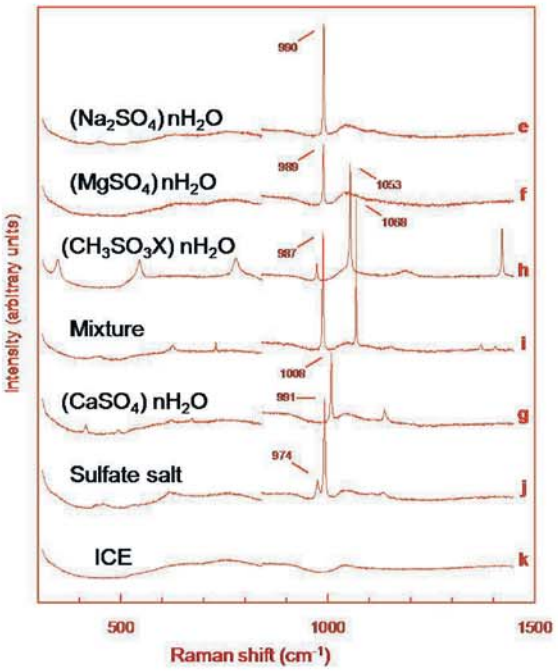

(b)

Fig. 3. Raman spectra of microparticles included in the Dome Fuji ice core [5]. The spectra **e** *to* ***i*** *in panel (b) correspond to the optical microscope images (e) to (i) in panel (a), respectively. The hydration number n, unknown species X and unknown sulfate salt j are to be presented and discussed by Sakurai [15].*

2. Behavior of gas molecules in ice sheets

Air bubbles trapped in ice sheets could yield precious information for paleoclimate reconstructions. However, during the transition from air bubbles to air hydrates, extremely high levels of gas fractionation

were found. Careful attention is therefore required in the interpretation of gas composition data obtained from gas analyses of ice cores. I will summarize briefly the mechanisms related to the fractionation process in the following subsections.

Concerning the terminology, an air hydrate is a transparent crystal in which air constituent gas molecules are trapped in polyhedral cages formed by hydrogen-bonded water molecules. This cage structure is called a clathrate, and air hydrates are also called clathrate hydrates. In the following subsections, however, the term "hydrate" is used for simplicity instead of air hydrate or clathrate hydrate.

2.1 Gas fractionation in the transition zone

Ikeda *et al.* carried out micro-Raman measurements on individual air bubbles and hydrates included in the Vostok ice cores, and they found very different compositions of N_2 and O_2 depending on air bubbles and hydrates as shown in Fig. 4 [1]. Hydrates in the transition zone have gas compositions enriched by O_2, while N_2 is enriched in air bubbles in the zone. Note that N_2/O_2 ratios averaged over all air bubbles and hydrates at each depth are equal to the atmospheric ratio of 3.7. They also proposed a molecular diffusion model between air bubbles and hydrates [1, 2], and Salamatin *et al.* developed a numerical model to explain the whole process quantitatively on the basis of the same model [3]. The N_2/O_2 ratios as a function of depth calculated by the model explained the data obtained by both the Vostok and Dome Fuji ice cores very well. In the following paragraphs the molecular diffusion model for the gas fractionation is briefly described according to the review article by Ikeda- Fukazawa and Hondoh [20],

The major process for the fractionation is molecular diffusion of N_2 and O_2 in an ice crystal. This process is

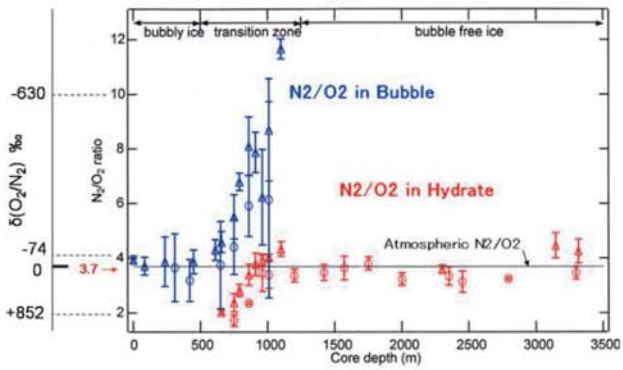

Fig. 4. Very large fractionation of N_2 and O_2 between air bubbles and clathrate hydrates found in the Vostok ice core [1]. Hydrates in the transition zone have gas compositions enriched by O_2, while N_2 is enriched in air bubbles in the zone. Note that the relative deviation from the atmospheric composition $\delta(O_2/N_2)$ is usually used in the literature instead of the ratio N_2/O_2.

very slow, as most of glaciologists think ice is impermeable for gas. However, not only N_2 and O_2 but also other larger molecules can migrate through the crystal structure of ice. Ikeda-Fukazawa carried out molecular dynamics simulations of various molecules in ice to deduce their diffusion coefficients [21].

Consider the case that both air bubbles and hydrates coexist in ice as shown in Fig. 5(a). First we define the dissociation pressure P^{d}_{Air} at which the three phases, ice, hydrate and air, are in equilibrium. Hydrates dissociate into air and ice at a pressure lower than P^{d}_{Air}, and *vice versa* at a pressure higher than P^{d}_{Air}. At P^{d}_{Air} the concentrations of N_2 and O_2 molecules dissolved in ice are kept constant anywhere in ice at X^{H}_{N2} and X^{H}_{O2},

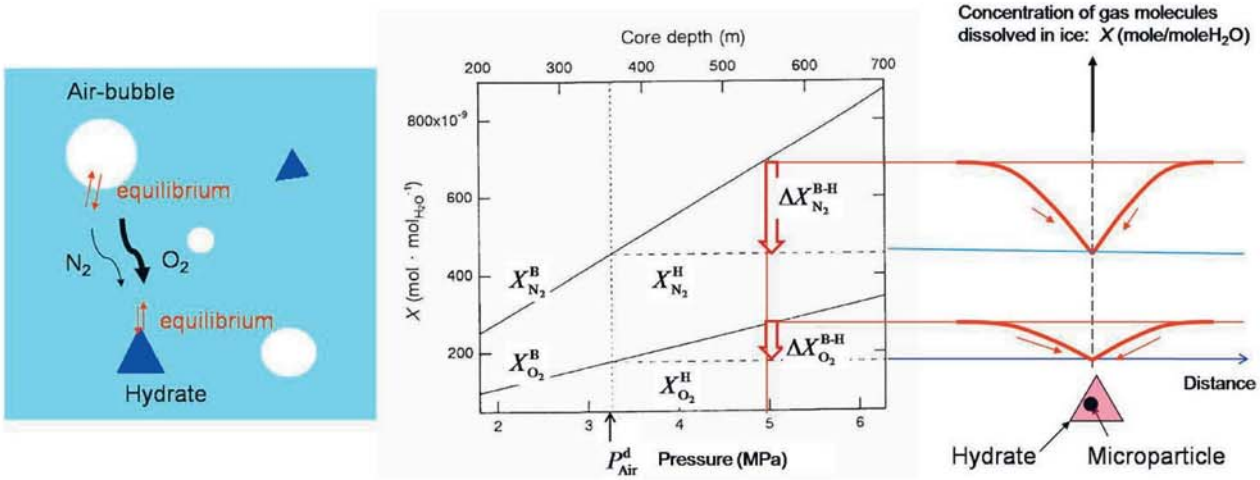

(a) (b) (c)

Fig. 5. A molecular diffusion model for gas fractionation in the transition zone.

respectively. (Note that this is a hypothetical case because actually there are no hydrates at the depth of the dissociation pressure P^{d}_{Air} in ice sheets.)

As the depth increases, the bubble pressure or the partial pressure P_i (i = N_2, O_2) increases, and consequently the concentrations of N_2 and O_2 molecules dissolved in ice X^{B}_{i} (in mole fraction) also increase as shown by the solid lines in Fig. 5(b), or

$$X_i^{\mathrm{B}} = k_i P_{\mathrm{i}} \quad (i = \mathrm{N}_2, \mathrm{O}_2)\,, \tag{1}$$

where k_i is Henry's constant. The two horizontal lines in Fig. 5(b) indicate the dissolved concentrations of N_2 and O_2 in equilibrium with hydrate, X^{H}_{N2} and X^{H}_{O2}, respectively. Since X^{H}_{N2} or X^{H}_{O2} varies proportionally with the composition ratio of i-molecules occluded in the cages of the clathrate structure Y_i, but does not depend on pressure and temperature significantly along the transition zone, it is given by

$$X_i^{\mathrm{H}} = k_i P_i^d Y_i \quad (i = \mathrm{N}_2, \mathrm{O}_2)\,. \tag{2}$$

In the transition zone, in which bubbles coexist with hydrates, a diffusive mass flux of i-molecules from bubbles to hydrates is driven by the concentration difference $\Delta X^{B\text{-}H}_{i}$ [20].

Due to a very slow diffusion process, we assume that the concentrations of i-molecules dissolved in ice close to the bubble surface and hydrate surface are kept equal to X_i^B and X_i^H, respectively. Considering a simple case in which a single hydrate is surrounded by many bubbles with the same partial pressure P_i, the diffusive mass flux of i-molecule q_i can be expressed in terms of the pressure difference as

$$\begin{aligned} q_i &\propto D_i k_i (P_i - P_i^d Y_i) \\ &\propto D_i k_i P_i^d \left(\frac{P_i - P_i^d Y_i}{P_i^d}\right), \end{aligned} \tag{3}$$

where D_i is the diffusion coefficient of i-molecules in ice, or it is defined by the time average of the square of the displacement. Since the mass flux driven by the pressure difference is proportional to the term $D_i k_i$ in eq. (3), this term is so called the "permeability constant". In the present case, however, we define the term $D_i k_i P_i^{d}$ in eq. (3) as the permeation coefficient D_i^{S} because P_i^{d} is also a material constant, and we prefer to use a non-dimensional expression for the pressure difference [3], specifically:

$$D_i^S = D_i k_i P_i^d\,, \tag{4}$$

or

$$q_i \propto D_i^S \left(\frac{P_i - P_i^d Y_i}{P_i^d}\right). \tag{5}$$

To understand the gas fractionation shown in Fig. 4, we have to know the difference between D_{N2}^{S} and D_{O2}^{S}.

Table 1. Diffusion coefficient D_i, Henry's constant k_i, and permeability coefficient D_i^S used for diffusion of gas molecules in ice [20].

	Ikeda *et al.* [2] (263K)		Salamatin *et al.* [3] (220K)	
	N_2	O_2	N_2	O_2
D_i (m²/s)	1.6 x10^{-13}	5.5 x10^{-13}	---	---
k_i (1/MPa)	1.8 x10^{-7}	2.6 x10^{-7}	---	---
P_i^{d} (MPa)	11.78	8.97	3.6	2.6
D_i^{S} (m²/s)	3.4 x10^{-19}	1.3 x10^{-18}	1.4 x10^{-21}	3.0 x10^{-21}

Although we have no experimental data on the permeation coefficients of N_2 and O_2, Ikeda estimated both D_i and k_i by a semi-empirical method [2], and also carried out the molecular dynamics simulations on the diffusive motion of N_2 and O_2 in ice [21]. Those estimated values are summarized in Table 1 [20]. Salamatin developed a mathematical model for the transition process, and obtained the permeation coefficients by constraining the model to the experimental data as shown in Table 1 [3, 22].

As a result, D_{O2}^{S} is 2 to 4 times larger than D_{N2}^{S}, and a higher diffusive flux for O_2 than for N_2 is concluded by substituting typical values for P_i and Y_i into eq. (3). Consequently, the N_2/O_2 ratios for hydrates become smaller than the atmospheric value, and *vice versa* for air bubbles. In a depth below the transition zone, the diffusion of gasses still takes place between hydrates with different diameters and N_2/O_2 ratios [23].

2.2 Nucleation of clathrate hydrates

In the discussion mentioned above, we regard the nucleation of hydrates at an air-bubble surface as quite natural, although we know that the nucleation probability is very small [24]. However, Ohno carried out detailed observations on distribution of both air bubbles and hydrates in the transition zone, and he found a nonuniform distribution of hydrates, unlike air bubbles that are distributed uniformly [25]. In addition to this fact, he also found that almost all hydrates include microparticles in the early stage of the transition zone [25]. These facts suggest that hydrates are preferentially nucleated on the microparticles but not on the air bubbles, at least in the beginning of the transition zone. The nucleation probability increases as the excess concentrations of N_2 and O_2 increase with increasing depth. Once a hydrate is nucleated on a microparticle surface, the dissolved concentrations of N_2 and O_2 drop to the values in equilibrium with the hydrate, as shown

in Fig. 5 (c). The hydrate grows by diffusive flow of N_2 and O_2 from air bubbles around it. Then, the fractionation results as described above.

According to the classical nucleation theory, a free energy barrier to be surmounted for the homogeneous nucleation of a clathrate hydrate in ice exceeds hundreds of eV, which is too large to activate the nucleation [26]. Therefore, we have to consider some heterogeneous effects on the nucleation. For simplicity, we do not consider the behavior of N_2 and O_2 separately in the following paragraphs on the hydrate nucleation. Note that the suffix "i" in this subsection refers to "ice" rather than N_2 or O_2, unlike in the preceding subsection.

A free energy increase by formation of a spherical nucleus with a radius r, as shown in Fig. 6(a), is given by

$$\Delta G = 4\pi r^2 \gamma_{\text{h-i}} - \frac{4}{3}\pi r^3 \frac{1}{\Omega_h} \Delta\mu_{\text{h-i}} , \qquad (6)$$

using the interfacial energy between hydrate and ice $\gamma_{\text{h-i}}$ and the volume of a water molecule in hydrate Ω_h. The chemical potential difference can be approximately expressed as

$$\Delta\mu_{\text{h-i}} \simeq kT\nu_h \ln\left(\frac{P}{P^d}\right) , \qquad (7)$$

where ν_h is a ratio of the number of cages to the number of water molecules in the clathrate structure, and it equals to 3/17 for the structure II [26].

For a heterogeneous nucleation, we first compare the two cases, nucleation on a microparticle shown in Fig. 6(b), and nucleation on a bubble surface shown in Fig. 6(d). For both cases the second term on the right-hand side of eq. (6) is the same, and so the first term is replaced by ΔG_M or ΔG_B, being equal to an increment in the free energy by formation of a nucleus.

For nucleation on a microparticle shown in Fig. 6(b), the free energy increment by formation of a disc with a radius R and thickness l is given by

$$\Delta G_M \simeq \pi R^2(\gamma_{\text{h-M}} - \gamma_{\text{i-M}}) + (\pi R^2 + 2\pi Rl)\gamma_{\text{h-i}} , \qquad (8)$$

where $\gamma_{\text{h-M}}$ and $\gamma_{\text{i-M}}$ are the interfacial energies between hydrate and microparticle, and ice and microparticle, respectively. Similarly for nucleation on a bubble surface,

$$\Delta G_B \simeq \pi R^2(\gamma_{\text{h}} - \gamma_{\text{i}}) + (\pi R^2 + 2\pi Rl)\gamma_{\text{h-i}} , \qquad (9)$$

where γ_{h} and γ_{i} are the surface energies of hydrate and ice, respectively.

Since the second term on the right-hand side of both equations (8) and (9) is identical, the difference between the two cases is due to a difference between ($\gamma_{\text{h-M}}$-$\gamma_{\text{i-M}}$) and (γ_{h}-γ_{i}). However, we can assume $\gamma_{\text{h-M}} \sim \gamma_{\text{i-M}}$ and $\gamma_{\text{h}} \sim \gamma_{\text{i}}$, because hydrate and ice might have a similar nature of surface. Therefore, these first terms can be neglected in these equations. Then, there is no significant difference

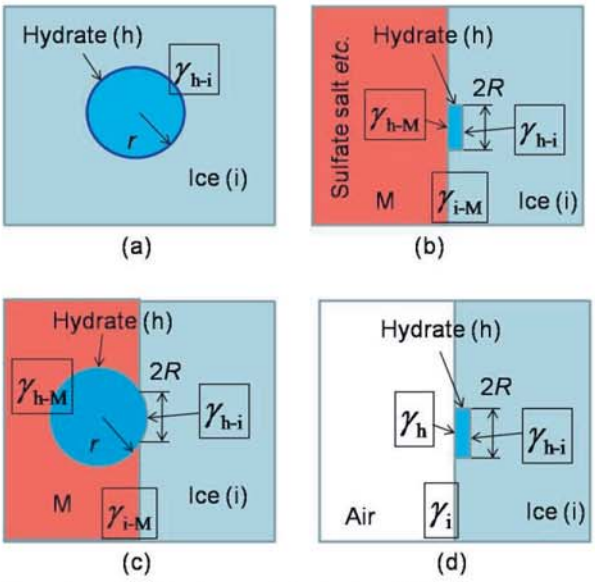

Fig. 6. Nucleation of hydrate. (a) Homogeneous nucleation, (b) heterogeneous nucleation of a disc with a radius R and thickness l on other materials such as sulfate salts, (c) heterogeneous nucleation in a micro-pit on other materials, (d) nucleation of a disc with a radius R and thickness l on air-bubble surface.

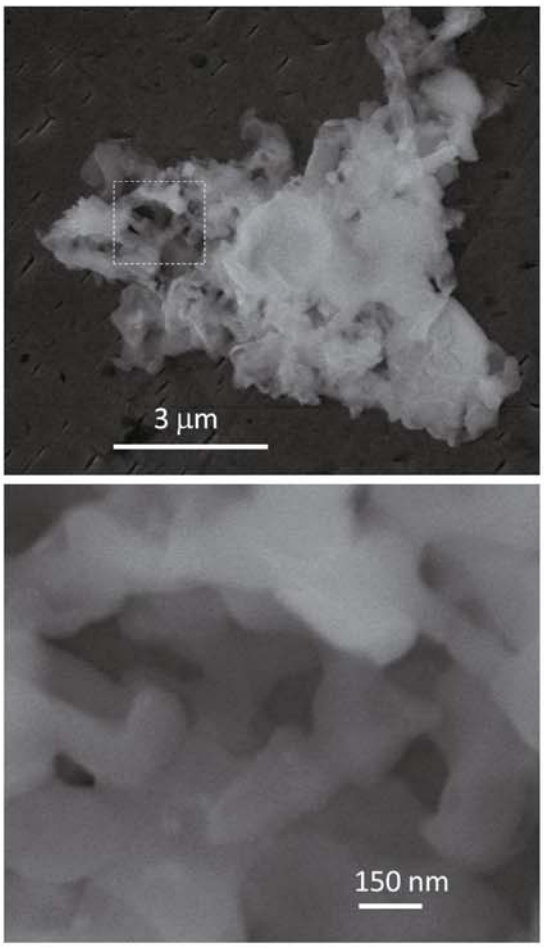

Fig. 7. FE-SEM images of a microparticle obtained by the sublimation method.

in the nucleation of hydrate in either case. However, it should be emphasized that the second term is too large to allow the hydrate nucleation, as discussed in my previous papers [24, 26]. Moreover, in addition to the observations by Ohno stated above [14, 25], Shimada confirmed acceleration of hydrate formation under higher concentrations of impurities [27]. Therefore, we have to introduce other impurity effects into the hydrate formation mechanism.

We consider a very special case of microparticles which have a very small interfacial energy with hydrate, or $\gamma_{h\text{-}M} \sim 0$, but a certain large interfacial energy with ice, so as to have the relation $\gamma_{i\text{-}M} \sim \gamma_{h\text{-}i}$. Then, eq. (8) becomes;

$$\begin{aligned} \Delta G_M &\simeq \pi R^2(\gamma_{h\text{-}i} - \gamma_{i\text{-}M}) + 2\pi Rl\gamma_{h\text{-}i} \\ &\approx 2\pi Rl\gamma_{h\text{-}i} \ . \end{aligned} \tag{10}$$

Consequently, ΔG_M depends only on $\gamma_{h\text{-}i}$, but neither on $\gamma_{h\text{-}M}$ nor on $\gamma_{i\text{-}M}$, and eq. (6) reduces to

$$\begin{aligned} \Delta G &\simeq 2\pi Rl\gamma_{h\text{-}i} - \pi R^2 l \frac{1}{\Omega_h}\Delta\mu_{h\text{-}i} \\ &\simeq \pi Rl(2\gamma_{h\text{-}i} - R\frac{kT}{\Omega_h}\nu_h \ln\left(\frac{P}{P^d}\right)) \ . \end{aligned} \tag{11}$$

Alternatively, we can also consider a rough surface of microparticles, which could provide preferential sites for the hydrate nucleation. By assuming a micro-pit on the surface as shown in Fig. 6(c), the free energy increment by hydrate formation can be reduced to

$$\Delta G_{MP} \simeq 4\pi r^2(\gamma_{h\text{-}M} - \gamma_{i\text{-}M}) + \pi R^2\gamma_{h\text{-}i} \ . \tag{12}$$

Since the term ($\gamma_{h\text{-}M}$-$\gamma_{i\text{-}M}$) is close to zero, ΔG_{MP} becomes very small for small R, so that ice can be spontaneously transformed into hydrate within a micro-pit. Then, this hydrate provides a particular surface with radius R for further growth of hydrate outward to the bulk of ice. Accordingly, the free energy change by the further growth of hydrate can be expressed by eq. (11), because this is just a special case to derive eq. (10).

The ratio P/P^d is about 1.2 at a beginning of the transition zone, and the interfacial energy $\gamma_{h\text{-}i}$ was determined as 60 mJ/m^2 [28]. Substituting these values into eq. (11), R should be larger than 46 nm for spontaneous growth of hydrate due to a negative value of ΔG. This critical radius R_c becomes smaller for a larger ratio of P/P^d. For example, R_c=12 nm for P/P^d =2.0, which corresponds to the middle of the transition zone.

Actually, microparticles found in ice cores have a very rough surface as shown in Fig. 7, which seems to have appropriate micro-pits or holes corresponding to the case of Fig. 6(c). There exist many different varieties in shapes and chemical compounds of microparticles which have different efficiencies for the hydrate nucleation. As P/P^d increases with depth, nucleation sites with lower efficiencies are activated, including air-bubble surfaces.

According to the above mentioned mechanism for the hydrate nucleation, we understand the results of various observations as follows:

(1) Nonuniform distribution of hydrates is due to a nonuniform distribution of microparticles, of which depth profiles have annual variations and others with longer wavelengths [14].

(2) A larger number-concentration of hydrates than that of air-bubbles is due to the hydrate nucleation at microparticles in addition to air bubbles [14].

(3) A very small value of N_2/O_2 of hydrates at the beginning of the transition zone as shown in Fig. 4 is due to the preferential nucleation of hydrates at microparticles. This has been a discrepancy between model prediction and ice core data [24, 25]. The model predicts the value equal to that of the atmosphere at the beginning of the transition zone because it assumes nucleation at air bubbles only. The model should be improved so as to include the nucleation process at microparticles.

(4) A large difference in appearance of hydrates reported in the previous papers [29, 30] could be explained by the difference in growth conditions of hydrates. When the hydrates are nucleated at microparticles under high supersaturation of gas molecules, polyhedral shapes are expected as a result of faceted crystal growth processes, because gas molecules are supplied from a dilute solid-solution of gas molecules in ice, like vapor growth of crystals [26]. Some very particular shapes, such as needle-like hydrates, must be due to certain specific gradients in the concentration of dissolved gas molecules around the growing hydrate, which might be caused by the specific distribution of air bubbles around it.

2.3 Recovery processes of ice cores during storage

(1) Dissociation of hydrates

Since hydrates gradually dissociate to air bubbles after pulling out ice cores from deep ice sheets, transparency of ice cores decreases with time as described by Miyamoto *et al.* in this volume [31]. The dissociation rate of hydrate strongly depends on storage temperature [32]: for example, 50% dissociation occurs after about 4 years at -20ºC, yet only 1% dissociation after about 6 years at -50ºC, and the same dissociation of 5% is reached after 115 days at -20ºC, while 34 years are required at -50ºC.

Such a surprisingly long life time of hydrates under atmospheric pressure can be explained as follows. If we assume that a hydrate crystal dissociates into an ice crystal and a gas bubble within a same volume, the pressure of the gas bubble strongly exceeds the dissociation pressure of the hydrate so that the hydrate

cannot dissociate. However, gas molecules might escape from the hydrate to ice core surfaces and other sinks by molecular diffusion in ice. When some part of the hydrate cages becomes empty of gas molecules, the hydrate lattice collapses into ice. Then, empty space appears because of the smaller volume of ice than hydrate. Gas molecules are supplied to the space from the hydrate until the bubble pressure reaches the dissociation pressure. Therefore, the bubble pressure must be kept at the dissociation pressure until all the hydrate dissociates to ice and gas, and the dissociation rate is limited by diffusion of gas molecules in ice. Since the diffusion coefficient of gas molecules in ice must have a large temperature dependence, the life time of hydrates strongly depends on the storage temperature as described above.

(2) Gas fractionation during storage

Since the pressure of a gas bubble being dissociated from hydrate is kept at the dissociation pressure (much higher than atmospheric pressure) as described above, diffusion of gas molecules takes place toward ice core surfaces. Then, fractionation of gases occurs similar to the case of the transition zone, which means preferential escape of O_2 than N_2 from the ice core. Ikeda *et al.* [33] modeled this process, and calculated the N_2/O_2 ratios as functions of storage temperature and time. Bereiter *et al.* [34] also calculated changes in CO_2 concentration and O_2/N_2 ratio for storage durations up to 38 years. These results agree with experimental measurements.

(3) Segregation of gas molecules and cloudy bands

Gas molecules dissolved in ice become excessive by depressurization after pulling out the ice from deep ice sheets. According to eq. (1), much smaller equilibrium concentrations of gasses must be attained, *e.g.*, about an one-hundredth reduction is required for ice pulled out from about 1100 m depth. Therefore, ice just after having been pulled out from deep ice sheets includes some amount of excess gas molecules, *e.g.*, N_2 and O_2 in the order of 10^{-10} mol are included in 1 mm^3 of ice. Moreover, additional gas molecules are supplied to ice from hydrates being dissociated.

These gas molecules segregate to sinks in the ice, although some parts of them escape to the atmosphere from surfaces of ice cores. Most effective sinks for gas molecules must be microparticles as mentioned in the preceding subsection, because their rough surface helps nucleation of gas bubbles in a similar way as for nucleation of hydrates. Then, micro-bubbles are formed around the microparticles. Since it is known that the number concentrations of the microparticles have annual variations, the micro-bubbles distribute corresponding to the annual layers, so that so-called cloudy bands are formed. The cloudy bands become gradually visible with time after pulling out the ice core from the deep ice sheet because of rather slow molecular diffusion in ice.

(4) Segregation and generation of self-interstitials

Summarizing the nature and behavior of intrinsic point defects (molecular defects) in ice may be useful for further understanding of ice core records. A crystal in general contains point defects in thermal equilibrium, of which concentrations can be expressed as functions of temperature T and pressure p,

$$C = \exp\left(\frac{S_f}{k_B}\right)\exp\left(-\frac{E_f + pV_f}{k_B T}\right), \qquad (13)$$

where E_f, V_f and S_f are the formation energy, formation volume and formation entropy of the point defect, respectively. For point defects in ice, we should distinguish those violating the ice rules (protonic defects) from those violating the lattice periodicity (molecular defects). The protonic defects, ion pairs and D-L pairs, largely determine the electrical properties of ice, while molecular defects are responsible for self-diffusion in ice.

Diffusion coefficients of the point defects are expressed by

$$D = D_0 \exp\left(-\frac{E_m + pV_m}{k_B T}\right), \qquad (14)$$

where E_m and V_m are the migration energy and

Table 2. Parameters of point defects and self-diffusion in ice [38].

	Point defects	Concentration at 0 °C C (in mole fraction)*	Formation energy: E_f	Diffusion coefficient: D	Migration energy: E_m
Protonic defects	D - L pair	4.0×10^{-7}	0.34 eV	1.4×10^{-9} m^2/s	0.24 eV
	Ion pair	5.5×10^{-12}	0.48	$\sim10^{-8}$	~ 0
Molecular defects	Self-interstitials	2.8×10^{-6}	0.40	2.0×10^{-9}	0.16
	Vacancy	$\sim 10^{-8}$	0.35		0.34
Self-diffusion	Self-diffusion coefficient (ice): D_{SD}			5.6×10^{-15}	0.60
	Self-diffusion coefficient (QLL on surface)			3.2×10^{-13}	0.24
	Self-diffusion coefficient (water)			1.3×10^{-9}	0.19

* 5.1×10^{-5} mol/mm^3 for Ice Ih.

Table 3. Self interstitial (SI) parameters for ice [35, 36, 38].

E_f (eV)	S_f	V_f	E_m (eV)	D_0 (m^2/s)	V_m
0.40	$4.9k_B$	-0.26Ω	0.16	1.8×10^{-6}	0.40Ω

Ω: molecular volume of ice ($3.26\times10^{-29}m^3$)

migration volume of the point defects, respectively. The concentrations and diffusion coefficients of the point defects in ice are summarized in Table 2 [35-38].

In ice, self-interstitials outnumber vacancies, so that $C_{SI} \gg C_V$ at least above –50 °C, and therefore the self-diffusion coefficient D_{SD} is approximately equal to the product of C_{SI} and D_{SI} measured separately, or $D_{SD} \approx C_{SI} D_{SI}$. The parameters for the self-interstitials in ice were determined by the x-ray topographic method as shown in Table 3 [35, 36].

Since self-interstitials become supersaturated by cooling according to eq. (13), excess self-interstitials should move away to a free surface or segregate to dislocation loops of interstitial type as shown in Figs. 8 (a) and (b) [39-42]. In contrast, dislocation loops of vacancy type (Figs. 8 (c) and (d)) are generated by heating as sources of self-interstitials to attain a higher concentration C_{SI} in ice [39-42].

For example, when ice is cooled down to -30 °C from 0 °C, the equilibrium concentration of self-interstitials decreases from 1.4×10^{-10} mol/mm^3 to 1.7×10^{-11} mol/mm^3, or supersaturation of about 800% is introduced. In contrast, supersaturation of only 2% is introduced by depressurization from 10 MPa to 0.1 MPa. Therefore, we consider the behavior of dislocations to be caused by temperature changes only.

The excess self-interstitials segregate into many dislocation loops, of which numbers and shapes depend on the cooling rate [39-42]. This process is rather fast; for example, the growth of dislocation loops ceases within one hour after a temperature change of about 10 °C. Then, the dislocation loops with stacking faults gradually shrink and disappear at a constant temperature because of the surface tension of stacking faults [40, 41]. This shrink process is rather slow; for example, it takes more than a day at -20°C for the loop radii of a few mm. In many cases, however, the dislocation loops without stacking faults remain after a long aging time at a constant temperature because a shrinkage force due to a line tension of a dislocation is too small to cause a climb motion of the dislocation for very large radii of the loops.

A similar behavior of dislocation loops of vacancy type were observed by heating as shown in Figs. 8 (c) and (d). In the case of vacancy type, however, multiple dislocation loops in Fig. 8 (d) should transform to a void as shown in Fig. 8 (e) when a strain energy due to the

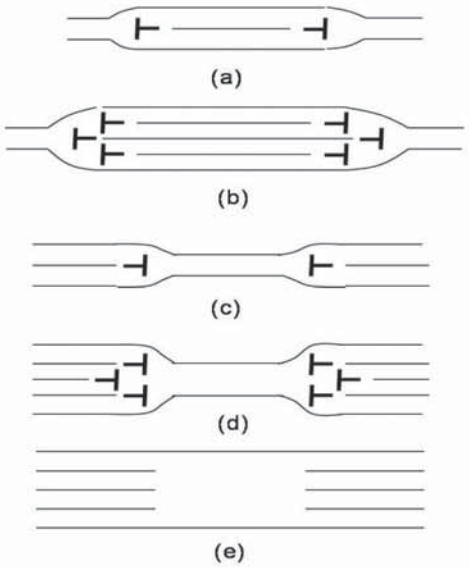

Fig. 8. Dislocation loops generated by temperature changes in ice: (a) a monolayer loop of interstitial type generated by cooling, (b) multiple loops of interstitial type generated by a rapid cooling, (c) a single loop of vacancy type generated by heating, and (d) multiple loops generated by a rapid heating. Pressurization introduces a vacancy type ((c) or (d)), while an interstitial type ((a) or (b)) is produced by depressurization. (e) A void can be formed when a strain energy due to the multiple dislocation loops exceeds the surface energy of a void. Note that stacking faults with the fault vector $\boldsymbol{p}+\boldsymbol{c}/2$ *are frequently observed [40] because this type of staking fault has the lowest fault energy [38], although the above figures are simplified without the horizontal displacement* $\boldsymbol{p}$.

multiple dislocation loops exceeds the surface energy of the void. This is the case for a rapid emission of SI's from the loops caused by a rapid heating. This mechanism provides formation of a disk-shaped void lying on the basal plane. Subsequently, gas molecules segregate to the void from hydrates being dissociated, and the void grows as a gas bubble.

All types of dislocation loops described above are invisible by an optical microscope, although their radii are as large as several mm. Experimental observations of the dislocation loops were carried out using laboratory-grown ice crystals by x-ray topography [41]. In contrast, a void (or gas bubble) are invisible by the x-ray topography but visible by an optical microscope because a void has no strain fields but it has a large difference in refractive indices from ice.

2.4 Fresh angles on firn densification and gas fractionation

It is well known that physical and chemical processes before and after precipitation on ice sheet surfaces can alter ice core records significantly, as

discussed by Iizuka *et al.* on chemical reactions in the atmosphere and surface firn [17], Ekaykin and Lipenkov on wind-driven redistribution of snow and post-depositional processes that alter isotopic compositions [43], Landais *et al.* on air mass transport related to d-excess and $^{17}O_{excess}$ [44] and Weiler *et al.* on isotope ratios and CO_2 concentrations in firn air [45] in this volume. In particular, firn densification is a key process to understand signals stored in ice cores. However, it includes complex physical processes such as structural rearrangement of ice grains, pressure sintering and plastic deformation. Salamatin *et al.* developed a new theoretical model of dry snow/firn densification in which all these physical processes were taken into consideration as included in this volume [46]. They deduced characteristic features of the densification process: for example, fractional contributions of grain rearrangement and plastic deformation of grains to a total compression rate as functions of depth.

On the other hand, during bubble close-off near the bottom of firn, air in open channels is progressively enriched with relatively small atoms and molecules. To understand the whole physical processes in firn, Fujita and others conducted a comprehensive study of the physical properties of firn cores at Dome Fuji, Antarctica [47]. They measured physical properties including (1) the relative dielectric permittivities in both the vertical and horizontal planes by the open resonator method, (2) the bulk density at a resolution of millimeters by the X-ray transmission method, (3) the three-dimensional geometric structure of pore space by the X-ray absorption microtomography, and (4) crystal orientation fabrics by the X-ray pole-figure analysis.

They found a very interesting behavior of firn as a function of depth. Firn near the surface of the ice sheet contains horizontal strata with thicknesses of several centimeters that are characterized by contrasting bulk density. Although density maxima exhibited a clear positive correlation with the strength of structural anisotropy and c-axis clustering around the vertical in the shallower part of the top 30 m, the correlation is reversed to negative in the deeper part. This means that initially low-density firn (ILDF) becomes denser than initially high-density firn (IHDF) in the deeper part by preferential deformation of weaker layers (ILDF). Then, the IHDF layers have their close-off at a deeper depth than those of the ILDF layers [47].

Prior to the above mentioned findings, Bender [48] discovered cyclic variations in $\delta(O_2/N_2)$, the relative deviation in the O_2/N_2 ratio from the atmospheric composition, in the Vostok ice core, which corresponded to changes in summer insolation at Vostok: low $\delta(O_2/N_2)$ occurred at times of high summer insolation. Kawamura *et al.* [49] found essentially the same relationship in the Dome Fuji ice core. They also found that the total air content (TAC) was synchronous with local summer solstice insolation: low TAC occurred at times of high summer insolation. Raynaud

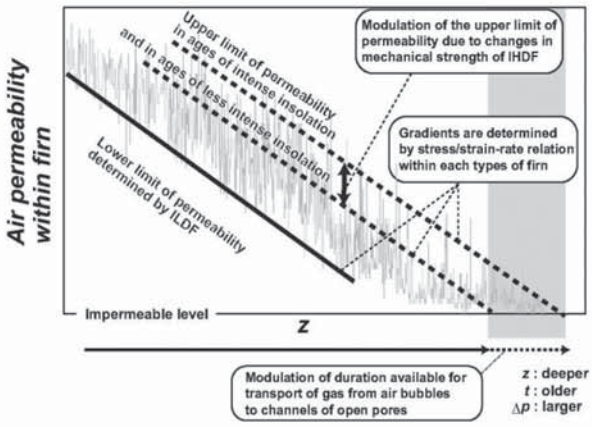

Fig. 9. Schematic diagram of the proposed mechanism for the modulation of conditions for gas diffusion near the bottom of firn in the ice sheet as a result of variations in local insolation. ILDF: Initially low-density firn. IHDF: Initially high-density firn [47].

et al. [50] presented changes in TAC of the EPICA Dome C ice core, and proposed that long-term changes in TAC recorded in ice from the high Antarctic plateau were dominantly imprinted by local summer insolation. Summarizing the results obtained so far; stronger local insolation leads to a smaller $\delta(O_2/N_2)$ and a smaller TAC.

For ice core chronologies, several different methods are used until now: identification of dated horizons along the cores, synchronization to other dated paleoclimatic records, counting of annual layers or modeling of the ice flow [51]. Lemieux-Dudon *et al.* proposed a new dating method with a probabilistic approach to construct an optimal ice chronology in this volume [51]. However, the correlation of local insolation with $\delta(O_2/N_2)$ and TAC has an invaluable advantage over other methods used in dating ice-cores [48-50, 52, 53], if the physical process to link the local insolation with the $\delta(O_2/N_2)$ and TAC is elucidated.

Severinghaus and Battle [52] and Kawamura *et al.* [49, 53] proposed models for the variations in $\delta(O_2/N_2)$ on the basis of gas fractionation caused by molecular diffusion from air bubbles to open channels. Since O_2 is preferentially extracted from pressurized bubbles as described in subsection 2.1, a smaller $\delta(O_2/N_2)$ is expected for a longer depth range of bubble close-off. A smaller TAC is also expected for a longer depth range of bubble close-off because more gas molecules are extracted from bubbles to open channels for a larger pressure difference between bubbles and channels and a longer diffusion time.

Based on the characteristic densification processes described above, Fujita *et al.* [47] proposed a model linking firn properties with conditions for the gas transport processes near the bottom of firn. The model

explains successfully how stronger local insolation leads to bulk ice with a lower $\delta(O_2/N_2)$ and a smaller TAC. According to their model, a stronger summer insolation increases the mechanical strength of IHDF layers, and therefore it increases the upper limit of permeability of the layers and the depth range of bubble close-off, as shown in Fig. 9. Hutterli *et al.* also discuss impact of local insolation on snow metamorphism [54].

Fujita *et al.* [47] suggested crushing events at Dome Fuji, or destructive deformation associated with vertical crushing in firn, on the basis of unusual dielectric anisotropy and unusual fragmented appearance of the structure in firn cores at a depth around 45 m. This crushing events and the reversal of density layers, ILDF and IHDF, described above are important to better understand the seasonal variations of various signals recorded in deep ice cores.

3. Behavior of various chemical trace species in ice sheets

3.1 Phase equilibria for chemical species in ice sheets

Various chemical species deposited on the ice sheet surface might be transformed towards phase equilibria, or towards the most stable state of ice, depending on different compositions of species and temperatures. We conducted a systematic survey of chemical species included in ice cores by using a micro-Raman spectrometer to determine chemical forms of microparticles, SEM-EDS for element analyses and ion chromatography for high resolution concentration profiles of various ions. The results obtained until now can be summarized as follows.

(1) Iizuka *et al.* [9] found that high-resolution concentration profiles of Na^+ and Mg^{2+} during the Holocene are almost identical with those of SO_4^{2-} except close to the ice sheet surface. This finding suggests that these ions form Na_2SO_4 and $MgSO_4$. In a similar way, Iizuka *et al.* [55] found high-resolution concentration profiles of Ca^{2+} well correlated with those of SO_4^{2-} during the LGM, suggesting the formation of $CaSO_4$. These suggestions were confirmed by micro-Raman measurements of the microparticles carried out by Ohno *et al.* [5]. Since they found poor correlations between cations (Na^+ and Mg^{2+}) and anions (SO_4^{2-}) in snow samples close to the ice sheet surface, they claimed that chemical reactions must take place to form the sulfate salts by a reaction of liquid H_2SO_4 with solid NaCl and $MgCl_2$ in surface snow. Iizuka *et al.* [9] also found that excess concentrations of anions (SO_4^{2-} and Cl^-) had uniform distributions for the case that concentrations of SO_4^{2-} exceeded total concentrations of cations (Na^+ and Mg^{2+}). This result strongly suggests that excess anions free from formation of salt microparticles uniformly disperse in ice to form solid solutions. Consequently, we can say that cations do not migrate after deposition while anions do in ice.

(2) By using the advantage of cations described above, Iizuka *et al.* [56] proposed a high time-resolution analysis of sodium ion concentration profiles as an indicator of seasonal sea ice extent around Antarctica in the Holocene.

(3) Since the salt microparticles found in ice cores have size distributions centered around several μm, which is much larger than aerosols in the atmosphere, these microparticles must be formed by coalescence or reactions of aerosol particles before and after deposition. In addition, the number concentration of the water-soluble microparticles is larger than that of the dust (water-insoluble microparticles) of about the same size [5]. Consequently, we should take into consideration the water-soluble microparticles as well as water-insoluble microparticles to better understand physical properties that could be affected by microparticles, as to be discussed in subsection 3.3.

(4) Iizuka *et al.* [7] deduced a diagram to determine major chemical forms in ice at a depth in which the concentrations of major ions are known. This diagram agrees very well with the results obtained by the micro-Raman measurements, and explains the reason why those chemical forms are dominant at a certain depth. In addition, Iizuka *et al.* [8] developed a new sublimation method to carry out a rapid analysis of many microparticles by the SEM-EDS analysis, and confirmed as predicted by the diagram that the major chemical form in LGM ice is $CaSO_4$ while Na_2SO_4 and $MgSO_4$ are predominant in Holocene ice. See the paper included in this volume for more details [17].

(5) A new mineral "meridianiite", or $MgSO_4 \cdot 11H_2O$, was found in the Dome Fuji ice core by Genceli *et al.* [57], although $MgSO_4 \cdot 12H_2O$ was assumed earlier. This finding suggests the importance of the phase equilibrium study of salt microparticles because different hydration numbers of sulfate salts must affect aerosol radiative forcing significantly.

(6) In case of the Greenland ice core, Sakurai *et al.* [58] found microparticles of $CaCO_3$ in the glacial ice, and $CaSO_4$ not only in the glacial ice but also in the Holocene ice. Careful attention has been paid on these compounds by paleoatmospheric researchers, because $CaCO_3$ reacts with acids to produce additional CO_2 which might disturb atmospheric CO_2 concentrations.

3.2 Eutectic depth

The salt microparticles described in the preceding subsections transform to a liquid state at a certain eutectic temperature, depending on the chemical species included in ice. For example, the eutectic temperatures of HCl, NaCl and Na_2SO_4 are -86.0°C, -21.2°C and -1.3°C, respectively. Since most cations exist in the chemical forms of sulfate, nitrate and carbonate salts of which eutectic temperatures are close to the melting temperature of ice, the original distributions of cations must be preserved as solid microparticles throughout almost the whole depth. However, Sakurai found very recently that the eutectic depth of the sulfate salts

becomes much shallower when the sulfate salts coexist with other acids [15].

Consequently, we need to know phase equilibrium states of a mixture of acids (H_2SO_4, HCl, HNO_3 and H_2CO_3), salts (chloride, sulfate, nitrate and carbonate salts) and water (H_2O). However, of course, some chemical species located very far from others cannot contribute to attain the phase equilibrium state. Assuming the diffusion coefficient of HCl in ice to be of the order of 10^{-10} m^2/s at 250K, the diffusion distance of HCl over thousand years becomes of the order of a meter. Therefore, the phase equilibrium state in ice sheets must be attained within a mixture (reaction) scale range of a meter. Please note that this does not mean mixing of all chemical species within this scale range; only anions move to attain the phase equilibrium state, as described above.

Although dry snow/firn is assumed in the above discussions, Moore and Grinsted [59] discuss ion fractionation caused by seasonal melting in this volume.

3.3 Fresh angles on grain boundary (GB) migration with microparticles

A depth profile of ice grain diameters is one of the fundamental data in ice core research. The average grain diameter increases with depth as a result of grain growth driven by GB energy. However, the depth profile shows in general significant decreases corresponding to cold climates (see for example [60-62]). Since higher concentrations of dust (water-insoluble microparticles) in a cold climate might suppress grain growth significantly, the decreases could be understood by the distribution of the dust. As described in the preceding subsection, however, the number concentration of the water-soluble microparticles is larger than that of the dust (water-insoluble microparticles) of about the same size. Therefore, water-soluble microparticles suppress the grain growth more effectively than dust. Moreover, we should take into consideration transformation of water-soluble microparticles to liquid droplets below their eutectic depths.

First, I will reconsider mechanisms for dragging effects of microparticles on GB migration. Since pinning effects of microparticles on GB migration have been studied by many authors, I will focus on the point that has not been considered until now. Although previous theoretical studies have established the effects of various inclusions (insoluble and soluble impurities, air-bubbles and clathrate hydrates) on grain growth in ice [60-63], we should take into account interaction with water-soluble microparticles in addition to the well-known inclusions.

GB migration is driven by a driving force per unit area of GB $\boldsymbol{F}$ due to GB curvature and the difference in strain energies stored in adjacent grains. Fig. 10 (a) shows a concave GB when the migrating GB encounters a microparticle. This negative curvature acts as a backward force for the GB migration and a forward

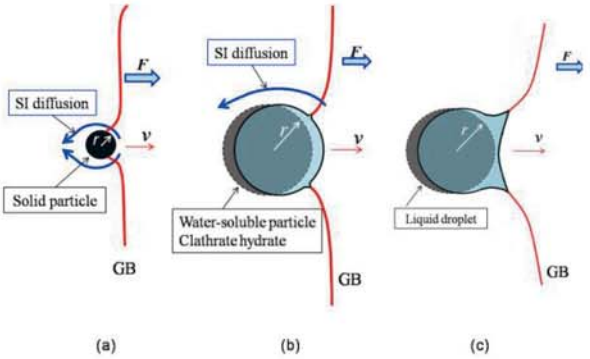

Fig. 10. Microparticle drags for grain boundary (GB) migration. (a) Water-insoluble microparticle (dust), (b) Water-soluble microparticle or clatharate hydrate, (c) Liquid droplet.

force for the microparticle. This force can be expressed as $\pi r \gamma_{GB}$ for the microparticle of radius r and the GB free energy γ_{GB} [63]. Then, an average normal stress applied on the front surface of the microparticle can be expressed as

$$\sigma = \frac{2\gamma_{GB}}{r} . \qquad (15)$$

Substituting γ_{GB} = 60 mJ/m^2 and r =1 μm, we obtain 0.12 MPa for the stress σ. This stress is sufficiently large to activate flow of self-interstitials (SIs), as shown

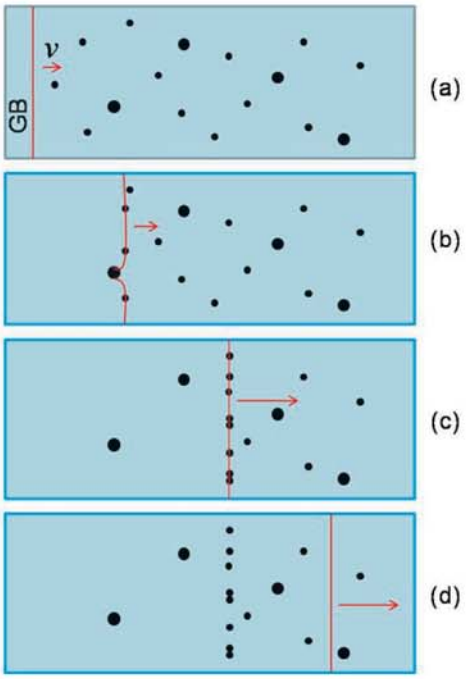

Fig. 11. Grain boundary (GB) migration in ice. Microparticles of which the radii are smaller than a critical radius r_c move together with the GB as shown in (a)-(c). Since r_c becomes smaller for a larger GB velocity v, microparticles are left behind the GB moving with a larger v as shown in (d).

in Fig. 10 (a). Then, the microparticle can move together with the GB unless $\boldsymbol{F}$ is larger than that required to separate GBs from microparticles, although it has been assumed in the literature that the microparticles do not move [61, 63]. Very slow migration of GBs together with microparticles should be taken into consideration because the growth process takes place over a long period of time.

Since a net flux of self-interstitials results by the forward force, the microparticle moves at a velocity v limited by the diffusive accommodation. Since a larger particle requires removal of a larger volume of ice in front of the microparticle and a longer diffusion distance, v becomes smaller for larger microparticles. Therefore, there exists an upper limit of radius r_c for a microparticle that can move together with a GB.

Fig. 11 illustrates schematically the behavior of microparticles with different diameters during GB migration. Microparticles of which the radii are smaller than a critical radius r_c move together with the GB, as shown in (a)-(c). Since r_c becomes smaller for a larger GB velocity v (larger driving force F), the microparticles lined up are left behind the GB of which the velocity becomes much larger than it was before, as shown in (d).

Alley *et al.* formulated the extrinsic effects on grain growth in three different cases: microparticle drag, bubble drag and impurity drag [63]. For microparticle drag, we should consider water-soluble microparticles and clathrate hydrates in addition to dust (water-insoluble microparticles). Fig. 10 (b) illustrates this case schematically. The microparticle moves together with the GB by growth and dissociation of the microparticle in addition to SI diffusion around the microparticle, as shown in Fig 10 (b). This additional growth/dissociation process increases the mobility of water-soluble microparticles and clathrate hydrates than the water-insoluble microparticles, although the process is still very slow.

Fig. 10 (c) shows an interaction of a liquid droplet with a migrating GB. In this case, migration of a droplet is caused by melting of ice in front of the droplet followed by freezing of water in the rear of the droplet. This process must be faster than the cases shown in Figs. 10 (a) and (b), and therefore many droplets can move with GBs. Consequently, coalescence of droplets happens to form larger droplets during GB migration. Fig. 10 (c) illustrates the case for the interface energy between the liquid and ice $\gamma_{i\text{-}l}$ being lager than $\gamma_{GB}/2$. In contrast, the liquid droplet should disappear to spread into GB if $\gamma_{i\text{-}l}$ is smaller than $\gamma_{GB}/2$. Sakurai found the former case in the Dome Fuji ice core [15].

For soluble-impurity drag, on the other hand, most of ions should be excluded because they form solid microparticles, as described above. Only a few anions such as Cl^-, SO_4^{2-} and NO_3^- being in excess from formation of salt microparticles should be considered as soluble impurities.

Taking all factors stated above into consideration, the extrinsic effects on grain growth should be reexamined. As a typical example, let us consider correlations of grain growth rates with concentrations of three different ions, Na^+, Mg^{2+} and Ca^{2+}. Since the major chemical form of water-soluble microparticles in LGM ice is $CaSO_4$ while Na_2SO_4 and $MgSO_4$ are predominant in Holocene ice [17], the concentration of Ca^{2+} shows a good correlation with the growth rates in LGM, and the sum of concentrations of Na^+ and Mg^{2+} dose in Holocene. However, these good correlations do not result from soluble impurity effects at all, but from microparticle effects.

4. Behavior of dislocations and ice sheet dynamics

The main purpose of this section is to summarize anisotropic deformation modes in ice in order to make a bridge between physics of atomistic structures of ice and glacier dynamics on a macroscopic scale. First I will briefly review the elementary theory of dislocations in ice according to the previous review article [38]. In the second step, applying the elementary theory, I will introduce a new picture of characteristic deformation modes in ice, which must be important to better understand the physical properties of ice cores and the dynamics of glaciers and ice sheets.

4.1 Possible Burgers vectors and slip systems in ice

The possible slip systems in a given crystal can be predicted by the following criteria [64].

(1) Low self-energy requirement

Since the self-energy of a dislocation E_d is proportional to the square of the Burgers vector length as expressed in eq.(16), only a few different types of dislocations with short Burgers vectors can exist in a real crystal.

$$E_d = \frac{Kb^2}{4\pi} \ln\left(\frac{\alpha R}{b}\right), \qquad (16)$$

where K is the energy factor expressed by the elastic constants, α the core parameter (approximately equal to 2 for ice), and R the outer cutoff radius. When a dislocation lies along the center of a cylinder, R equals it's radius. For a regular dislocation array in a small angle grain boundary, R is half of the dislocation spacing. Thus, the self-energy E_d depends on the sample size and the dislocation arrangement. The energy factor K equals μ for screw dislocations and $\mu/(1-\nu)$ for edge dislocations in isotropic continua, where μ and ν are the shear modulus and the Poisson ratio, respectively. Burgers vectors and relative energies of possible dislocations in ice are listed in Table 4.

(2) Low Peierls stress requirement

The Peierls stress τ_p is the maximum lattice

resistance stress for glide motion of a dislocation, and according to the Peierls-Nabbarro model it is given by

$$\tau_p = \frac{2\mu}{1-\nu}\exp\left(-\frac{2\pi}{1-\nu}\cdot\frac{d}{b}\right), \qquad (17)$$

where d is the spacing of the glide planes and b the Burgers vector length [64]. The magnitude of the Peierls stress changes drastically with the value of d/b, and hence depends on the crystal structure. Therefore, because low-index planes have a larger lattice spacing d, dislocation glides on low-index planes are predominant over those on higher index planes.

For ice, basal planes {0001}, two types of prismatic planes $\{1\bar{1}00\}$ and $\{\bar{1}\bar{1}20\}$, and two types of pyramidal planes $\{\bar{1}011\}$ and $\{\bar{1}\bar{1}22\}$ have relatively large d. Considering possible Burgers vectors of the perfect dislocations listed in Table 4, possible slip (glide) systems, combinations of slip directions and slip planes, in ice can be summarized as shown in Fig. 12 [38].

(3) Stacking fault restriction

When the energy of a stacking fault lying on a certain lattice plane is sufficiently low, the dislocation extends into a ribbon-like structure on the lattice plane. The motion of the extended dislocation is strongly restricted on the plane of the extension. This restriction is very strong in ice, as described in the following subsections.

4.2 Why is the basal slip system predominant over all other slip systems?

If all slip systems shown in Fig. 12 were equally active in the deformation of ice, plasticity of ice should be much more isotropic. Therefore, the third criterion (stacking faults) should be considered. As discussed in the previous review [38], since the stacking fault on the basal plane has a very low energy in ice, a complete understanding of dislocation behavior in ice involves partial dislocations. A perfect dislocation $\boldsymbol{b}$ must dissociate into partial dislocations with smaller Burgers vectors $\boldsymbol{b}_1$ and $\boldsymbol{b}_2$ provided that $b^2 > b_1^2 + b_2^2$, and the energy of stacking faults associated with this dissociation is sufficiently low.

All of the perfect dislocations lying on the basal planes are stabilized by dissociating into two partial dislocations. The separation of the two partial dislocations in equilibrium w in Fig. 13 is calculated by equating the repulsive force between the two partial dislocations with the attractive force due to the stacking fault. The calculated equilibrium separations in ice are extremely large compared to those in other materials. This is because the widths for ice are more than several ten times the Burgers vectors, while those for metals and semiconductors are only about several times the Burgers vectors.

Consequently, all types of dislocations in ice are widely extended on the basal planes. It requires a very large stress to shrink the extended dislocations [37]. In

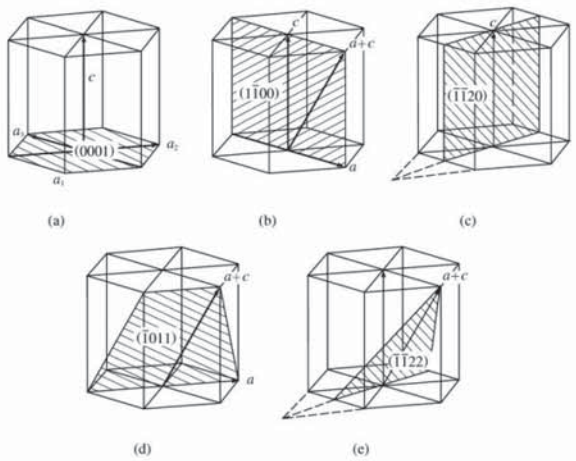

Fig. 12. Possible slip (glide) systems in ice [38].
(a) ***Basal****: <11$\bar{2}$0>/{0001}*
(b) ***Prismatic****: <11$\bar{2}$0>/{1$\bar{1}$00}, <0001>/{1$\bar{1}$00} and <11$\bar{2}$3>/{1$\bar{1}$00}*
(c) ***Second Prismatic****: <0001>/{$\bar{1}\bar{1}$20}*
(d) ***Pyramidal:*** *<11$\bar{2}$0>/{$\bar{1}$011} and <11$\bar{2}$3>/{$\bar{1}$011}*
(e) ***Second Pyramidal****: <11$\bar{2}$3>/{$\bar{1}\bar{1}$22}*
**Notation: <slip direction>/{slip plane}, where <hkil> and {hkil} express groups of equivalent directions and planes, respectively.*

Table 4. Burgers vectors of dislocations in ice [38].

Type of dislocation	Burgers vector		Self-energy (relative to $\boldsymbol{a}$)
Perfect	$\boldsymbol{a}$	0.452 nm	1
	$\boldsymbol{c}$	0.736 nm	2.7
	$\boldsymbol{a}+\boldsymbol{c}$	0.863 nm	3.6
Partial	$\boldsymbol{p}$	0.261 nm	0.33
	$\boldsymbol{c}/2$	0.368 nm	0.66
	$\boldsymbol{p}+\boldsymbol{c}/2$	0.451 nm	1.0

$\boldsymbol{a} = (1/3)\langle 11\bar{2}0\rangle$ $\quad$ $\boldsymbol{p} = (1/3)\langle 10\bar{1}0\rangle$
$\boldsymbol{c} = \langle 0001\rangle$ $\quad$ $\boldsymbol{p}+\boldsymbol{c}/2 = (1/6)\langle 20\bar{2}3\rangle$
$\boldsymbol{a}+\boldsymbol{c} = (1/3)\langle 11\bar{2}3\rangle$

* See subsection 4.2 for the two types of dislocations: perfect and partial dislocations.

exceptional cases, however, there exist short segments of perfect dislocations lying on the non-basal planes and perfect dislocations lying on the basal plane near a free surface [37]. Dislocations in an arbitrary direction within a crystal should have a terrace-like structure (or a stable configuration) such as shown in Fig. 14 (a). Under deformation, the most preferable configurations are those shown in Figs. 14 (b) and (c); *i.e.*, a short dislocation segment gliding on a non-basal plane followed by a dislocation dipole lying on the basal

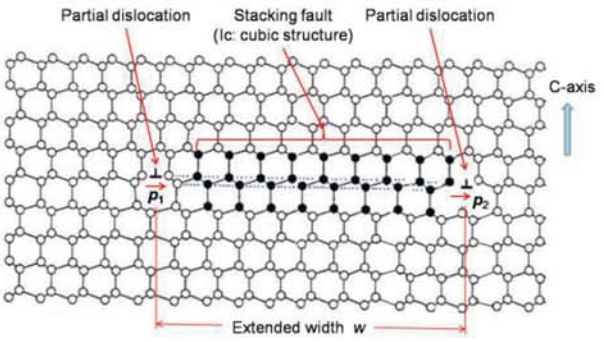

Fig. 13. An extended dislocation formed by dissociation of a perfect dislocation $\boldsymbol{a} = (1/3)\langle 11\bar{2}0\rangle$ *into two partial dislocations* $\boldsymbol{p} = (1/3)\langle 10\bar{1}0\rangle$ *with a stacking fault lying on the basal plane [37]. The open circles denote the oxygen atoms in a stacking sequence of the hexagonal ice Ih while the filled circles denote those in the cubic ice Ic. The extended width w is 55 nm for the edge dislocation in ice [37,38].*

planes are generated preferentially [37, 38]. In contrast, all slip systems becomes active close to a free surface. Accordingly, only near a free surface, pure screw dislocations can cross slip from the basal plane to a non-basal plane, *vice versa* [37, 41].

Since several molecular layers of the cubic structure I_c occur by introducing a stacking fault [38, 41], we can say that the unusual nature of dislocations in ice described above originates in the very small energy difference between hexagonal ice I_h and cubic ice I_c, although I_h is more stable than I_c at all temperatures.

4.3 Fundamental deformation modes of ice

We consider the three typical cases for plastic deformation of ice under uniaxial compression, as shown in Fig. 15. As it was well established in the 1950's and 1960's by very many experiments, ice can be deformed easily only in case (c) but hardly deforms in case (a). The case (b) is also hard to deform, but some extent of slip deformations were suggested by observations of slip lines on the surface. Dislocation mechanisms responsible for these three typical cases are discussed as follows.

(1) Uniaxial deformation parallel to the c-axis: Case (a)

A dislocation mechanism responsible for this case was depicted as shown in Fig. 16 by Hondoh [38]. Only pyramidal slip systems among the slip systems shown in Fig. 12 are responsible for this case. A short segment of screw dislocation with the Burgers vector $\boldsymbol{a}+\boldsymbol{c}$ glides on a pyramidal plane, followed by an edge dislocation dipole lying on the basal planes. Then, a local shear deformation occurs as shown in Fig. 16. However, this slip plane does not extend its area because the dislocations generated on the basal planes are sessile, or cannot glide at all. Successive generation of dislocation dipoles from the same source at surface or grain

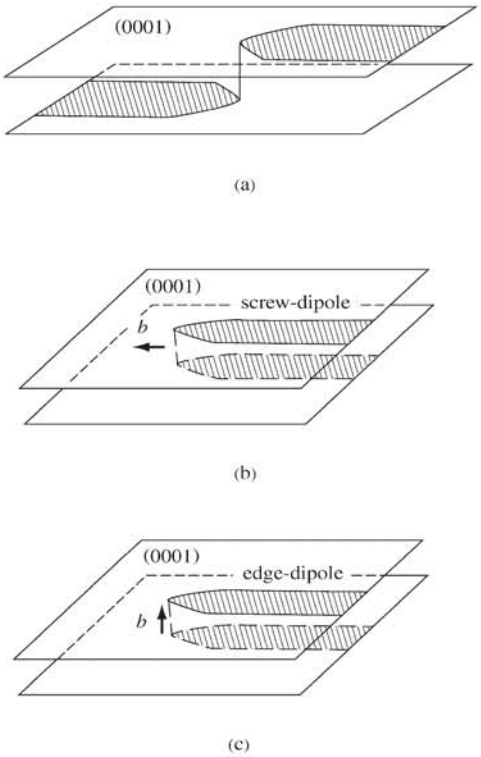

Fig. 14. Possible configurations of dislocations in ice: (a) stable configuration, (b) and (c) two possible structures of dislocation dipoles responsible for deformation of ice [38].

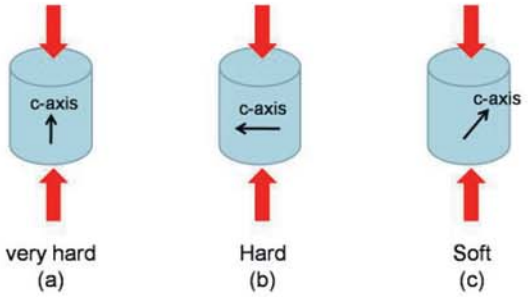

Fig. 15. Three different cases for uniaxial deformation. The classification "soft", "hard" and "very hard" are to be clarified in terms of dislocation behaviors described in subsection 4.3 and in Fig. 21.

boundary is suppressed by the sessile dislocations. Instead, similar local slips occur by chance at many other places in the specimen, so that many discontinuous slip planes are left. In this deformation mode, therefore, the generated dislocations with the Burgers vector of $\boldsymbol{a}+\boldsymbol{c}$ contribute little to the deformation of the whole specimen.

Since the dislocation $\boldsymbol{a}+\boldsymbol{c}$ can be dissociated into two dislocations $\boldsymbol{a}$ and $\boldsymbol{c}$ as shown in Fig.17 (b), the dislocation $\boldsymbol{a}$ can glide on the basal plane by a repulsive force between successively generated dislocations $\boldsymbol{a}$, in spite of no applied shear stress on the basal plane. Since

many different pyramidal slip systems are active, a characteristic deformation such as shown in Fig. 17 (d) becomes possible. Note that there is no deformation parallel to the compression axis in both Figs. 17 (c) and (d). Instead, a very large tensile stress concentration occurs at the center of the figure, and therefore cleavage cracks appear parallel to the basal planes although a compressive force is applied (A. Miyamoto, private communication). Successive generation of dislocations must wait until the concentrated stresses will be released by generation of cracks and/or climb motion of dislocations ***c***. Then, the specimen deforms in the direction of the compression axis. Since such a climb motion of dislocations requires diffusion of water molecules, the deformation rate is very small in this case, which is well known from the laboratory experiments [65].

As a result of relaxation processes of the dislocation arrangements described above, edge dislocation arrays are left as shown in Fig. 17 (e). This process provides a formation mechanism of small-angle tilt GBs lying on the basal planes.

(2) Uniaxial deformation normal to the c-axis: Case (b)

Both prismatic slip systems and pyramidal slip systems become active in this case. For the latter, the same argument as for case (a) holds. For the former, a responsible dislocation mechanism is shown in Fig. 18; *i.e.*, an edge dislocation segment gliding on a non-basal plane followed by a screw dislocation dipole lying on the basal plane governs the deformation in this case. This mechanism is similar to the case (a), but it has an important difference in that dislocations of the dipole with the Burgers vector ***a*** are glissile on the basal planes. Therefore, successive generation of the dislocation dipoles activates the basal slip systems in spite of no applied shear stress on the basal planes.

The same dislocation mechanism as for the pyramidal slip systems shown in Fig. 17 must be active in this case too, but contribution of the pyramidal slip system to a total deformation can be neglected compared to the prismatic slip systems because of its very slow process as described above.

In the case (b), therefore, the specimen deforms by cooperative operation of non-basal slip systems and the basal slip system as shown in the photograph of an ice surface in Fig. 19 [66]. However, generation of the dislocation dipole follows a sort of random process at surfaces (or grain boundaries), and therefore there are no entire slip planes, unlike the case (c) to be described. This is the reason why prismatic deformation is hardly observed in ice, in spite of faster movement of dislocations on the prismatic planes compared to those on the basal planes.

(3) Uniaxial deformation inclined to the c-axis: Case (c)

All slip systems are active in this case because shear stresses are exerted not only basal planes but also prismatic and pyramidal planes. A typical explanation for basal glide in ice is shown in Fig. 20 (a). According

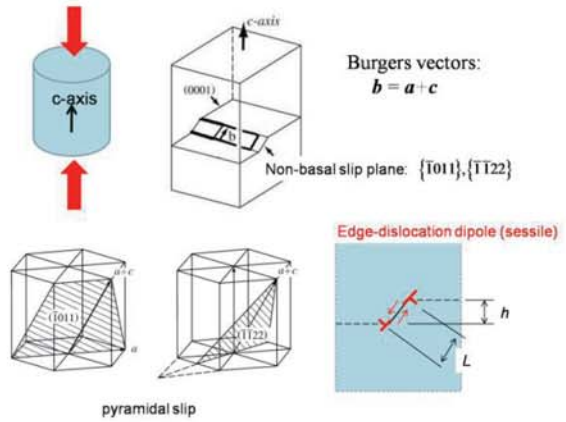

Fig. 16. A possible dislocation mechanism for the uniaxial deformation parallel to the c-axis (case (a) of Fig. 15).

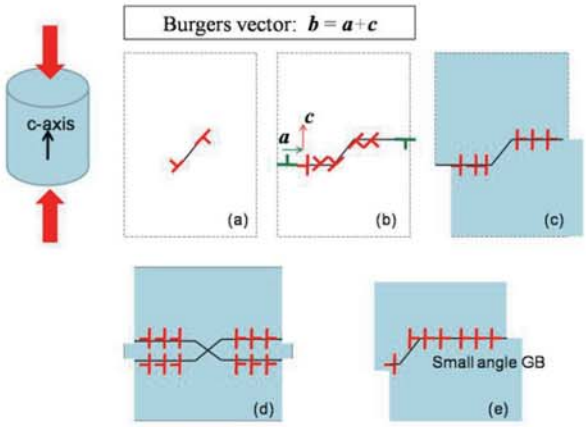

Fig. 17. Possible dislocation arrangements formed by further uniaxial deformation parallel to the c-axis.

to the results by x-ray diffraction topography, however, this is not the predominant dislocation mechanism for the actual deformation process of ice. Owing to much faster movement of non-basal glide than glide on the basal planes [66], generation of the dislocation dipoles is predominant in this case, as it is also shown in Figs. 20 (b)-(d). Dislocation velocities and other parameters for glide motion of dislocations in ice are summarized in the previous review article [38].

Since, unlike the former two cases, entire slip across the whole specimen is possible in either case of Fig. 20 (a) or (c), ice can be easily deformed in this case, which is thus designated an easy glide or easy deformation mode. However, it is worthwhile to emphasize that the basal glide is introduced by the non-basal dislocations, and almost all slip systems are activated even in the easy deformation mode. The contributions of these non-basal dislocations to the entire deformation are very small because of the short segmented dislocations.

According to the above mentioned mechanisms, dislocation dipoles should be generated first for all cases.

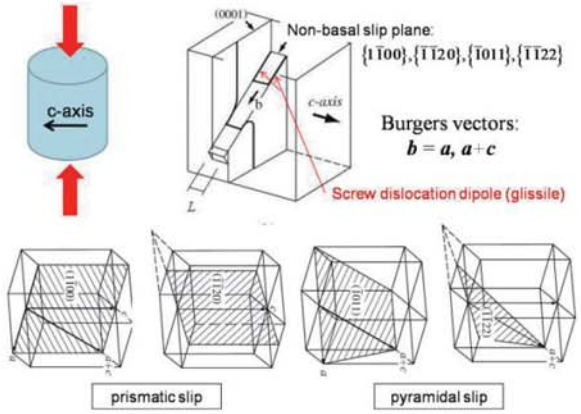

Fig. 18. A possible dislocation mechanism for the prismatic slip systems (case (b) of Fig. 15).

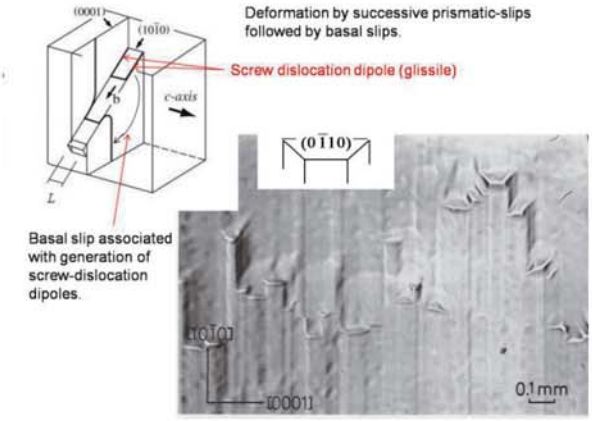

Fig. 19. Characteristic deformation by the prismatic slip systems. Successive generation of dislocation dipoles causes macroscopic deformation as shown by a hill-like structure on the surface (after J. Muguruma) [66]. The vertical thin lines must be caused by the basal slips as illustrated in the inset, so that they connect the discontinuous prismatic slip planes.

The distance between dipoles L in Fig. 16 is inversely proportional to the shear stress τ on the non-basal plane as

$$L \simeq \frac{\mu b}{\tau} . \qquad (18)$$

For the Burgers vector $\boldsymbol{a}$ and $\tau = 0.1$ MPa, the distance L is equal to about 10 μm. In case (c), this distance approximately corresponds to separation distances of slip lines observed on ice surfaces.

4.4 Strain energy stored in ice by deformation

As described in the preceding subsection, ice deforms in a very characteristic way depending on the deformation modes. As a summary of the rather complicated arguments in the preceding subsection, strain rates of ice and strain energies stored in ice by deformation with different orientations are summarized in Fig. 21. In the case of uniaxial deformation parallel to the c-axis, ice hardly deforms, but a very large strain energy can be stored in ice because unstable dislocation arrangements are generated by the deformation.

Considering the above-mentioned mechanisms, we can say that the strain energy stored in ice cannot be expressed in terms of densities of dislocations included in ice. It is possible that ice contains very high-energy dislocation configurations with rather low densities of dislocations. The configurations in Figs. 17 (c) and (d) have very much larger strain energies than small angle grain boundaries even if these configurations have the same dislocation density.

4.5 Formation of small-angle grain boundaries

Dislocations generated by deformation interact and react to form a new configuration of lower energy. This reaction is driven by interaction forces between the dislocations, and it requires diffusion of water molecules (SIs) in many cases. As a result of the reaction, small-angle GBs (sub-GBs) are formed if temperature is sufficiently high to activate the diffusion of SIs. In case of ice, stable small-angle GBs should be composed of only dislocations lying on the basal planes, of which the Burgers vector is $\boldsymbol{a}$ or $\boldsymbol{c}$, because only short segmented dislocations can exist on non-basal planes. Therefore, we should consider the following three cases for stable small-angle GBs in ice.

(1) Twist GB parallel to the basal plane: a dislocation net composed of two sets of screw dislocations with the Burgers vector $\boldsymbol{a}$. The rotation axis is normal to the GB plane, or parallel to the c-axis. Small-angle GBs of this type can be formed by all three deformation modes

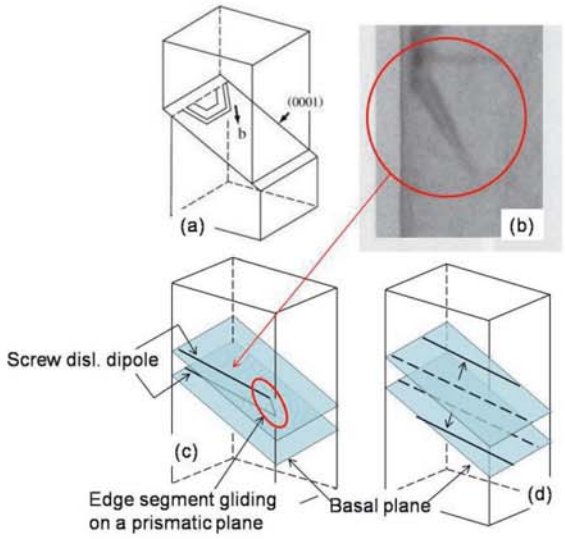

Fig. 20. A dislocation mechanism for the uniaxial deformation inclined to the c-axis, (case (c) of Fig. 15). Note that the dislocation mechanisms described in the cases (a) and (b) are also active in this case.

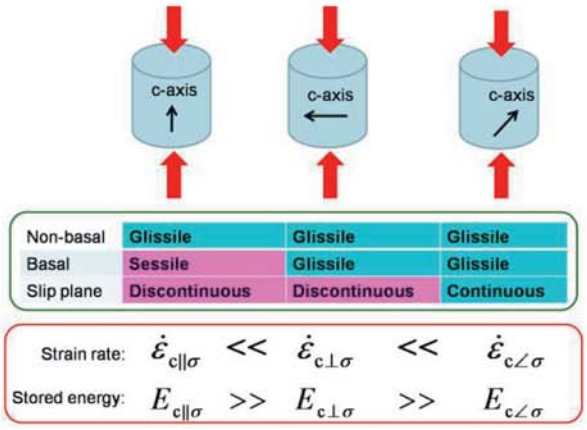

Fig. 21. Strain rates and stored energies in ice deformed in different orientations. Three different cases shown in Fig. 15 can be classified in terms of the dislocation behaviors: glissile or sessile dislocations, and continuous or discontinuous slip planes (see text for the detail of the mechanisms). Note that dislocations on non-basal planes are short segments of which lengths are expressed by eq. (18).

shown in Fig. 15.

(2) Tilt GB approximately parallel to the basal plane: a dislocation array composed of edge dislocations with the Burgers vector ***c***. The rotation axis lies on the basal plane. Small-angle GBs of this type can be formed only in the deformation mode (a) in Fig 15. The formation mechanism is schematically shown in Figs. 16 and 17. For a grain including small-angle GBs of this type, a stress must have been exerted to activate the pyramidal slips.

(3) Tilt GB normal to the basal plane: vertically aligned edge dislocations with the Burgers vector ***a*** lying on the different basal planes. There are two cases for the GB plane: $\{1\bar{1}00\}$ and $\{\bar{1}\bar{1}20\}$. In the former case, screw components are included in the dislocation array, while the dislocation array is composed of pure edge dislocations in the latter case. Small-angle GBs of this type can be formed by all three deformation modes shown in Fig. 15.

It should be emphasized that a twist GB normal to the basal plane is not stable because it requires screw dislocations lying on the non-basal planes. Moreover, in addition to the above three cases, there are many other possible configurations for dislocation walls in ice under deformation, although their dislocation structures must change towards one of the three stable structures during aging without further deformation.

4.6 Fresh angles on recrystallization

As pointed out by Jacka and Li [67], a small-circle girdle crystal orientation fabric can be formed instead of a single maximum in uniaxial deformation tests for a certain range of temperatures and stresses. This behavior of fabrics can be well understood if we take into consideration strain energies stored by deformation, as described in Fig. 21. A large strain energy is stored in a grain with c-axis oriented parallel to the deformation axis if the applied stress is large enough to activate the dislocation mechanism shown in Fig. 17. In addition to this condition, if the temperature is high enough for recrystallization, the grains with c-axis parallel to the deformation axis should disappear because of large strain energies stored in the grains, and then a small girdle fabric is formed.

It should be emphasized that all slip systems should be considered to better understand the fabric evolution in ice sheets, although only basal slip systems have been considered so far. Formation of small-angle GBs, for example, can be understood as a result of non-basal slips as described in the preceding subsection and by Weikusat *et al.* in this volume [68]. Montagnat *et al.* [69] and Svensson *et al.* [70] also discuss dislocation substructures formed in recrystallization processes.

Moreover, Donoghue and Jacka [71] show in this volume that the depths at which stress changes from predominantly near-vertical compression to predominantly near-horizontal simple shear zones can be detected by stress patterns within the Law Dome ice cap on the basis of crystal fabric data. According to Jacka and Li [72], the steady-state (or equilibrium) crystal size decreases with an increase in octahedral shear stress as a result of a "balance" between the grain growth and the deformation. These results strongly suggest that the effect of the flow itself on grain size should be taken into consideration in addition to the normal grain growth.

5. Radio-echo sounding based on dielectric properties of ice

Recent development of new methods in radio-echo sounding on ice sheets provides also typical examples of microphysics successfully applied to macroscopic scale phenomena, see for example Refs. [73-76].

Frequency dependence of dielectric properties of ice was applied to detect internal layers due to changes in acidity and in crystal-orientation fabric, separately. The Internal reflection layers due to changes in acidity are useful to calculate accumulation rates in the past, while those due to crystal orientation fabric are important for ice sheet flow analyses [74, 75]. Moreover, it was suggested by Fujita *et al.* [76] that birefringence occurring on a macroscopic scale within ice sheets can be applied to detect internal sub-structures related to past ice sheet flow. Multi-frequency methods and polarization methods in radio-echo sounding must be powerful tool to extend information obtained from ice cores over a wide ice sheet area.

6. Summary: toward nanoglaciology

The physical properties of ice cores have been recognized as important fundamental data in ice core research; however, it has also been recognized that for the purpose of paleoclimatic and paleoenvironmental reconstructions, these data are less important when compared to the isotope, gas and chemical analysis data. Nevertheless, as described in this overview, microphysical ice sheet processes become important not only to better our understanding of the signals recorded in ice cores, but also to deduce information invaluable to paleoclimatic and paleoenvironmental reconstructions. Moreover, the dislocation mechanisms for different deformation modes provide the fundamental understanding needed for modeling the anisotropic flow dynamics of ice sheets.

Great progress has been made in this decade through the use of laboratory equipment designed for application to materials science. From this versatility we should learn the importance of integrating different disciplines. Faria [77], Faria *et al.* [78] and Kirchner and Faria [79] discuss multidisciplinary ice core research and the multiscale structures of Antarctica, while Gagliardini *et al.* refer to flow/deformation modeling on different scales [13].

As schematically illustrated in Figs. 22 and 23, new prospects in glaciology can arise by bridging the gap between macroscopic phenomena in glaciology and physical processes taking place on a nanometer scale, and we call this *nanoglaciology*. However, since nanoglaciology should cover various phenomena at very different scales as shown in Fig. 22, a structural hierarchy must be considered. In the case of ice sheet dynamics, for example, there are several different levels within the structural hierarchy varying from nanometer to kilometer scales as shown in Fig. 23.

At the base of the hierarchy in Fig. 23, the positions of a number of molecules have to be described for a plastic deformation. Although molecular dynamics

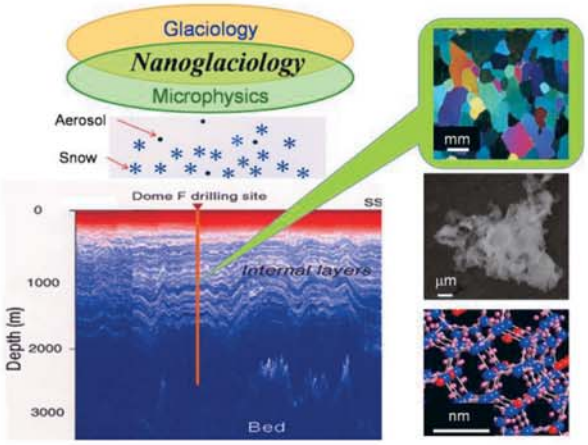

Fig. 22. Toward nanoglaciology.

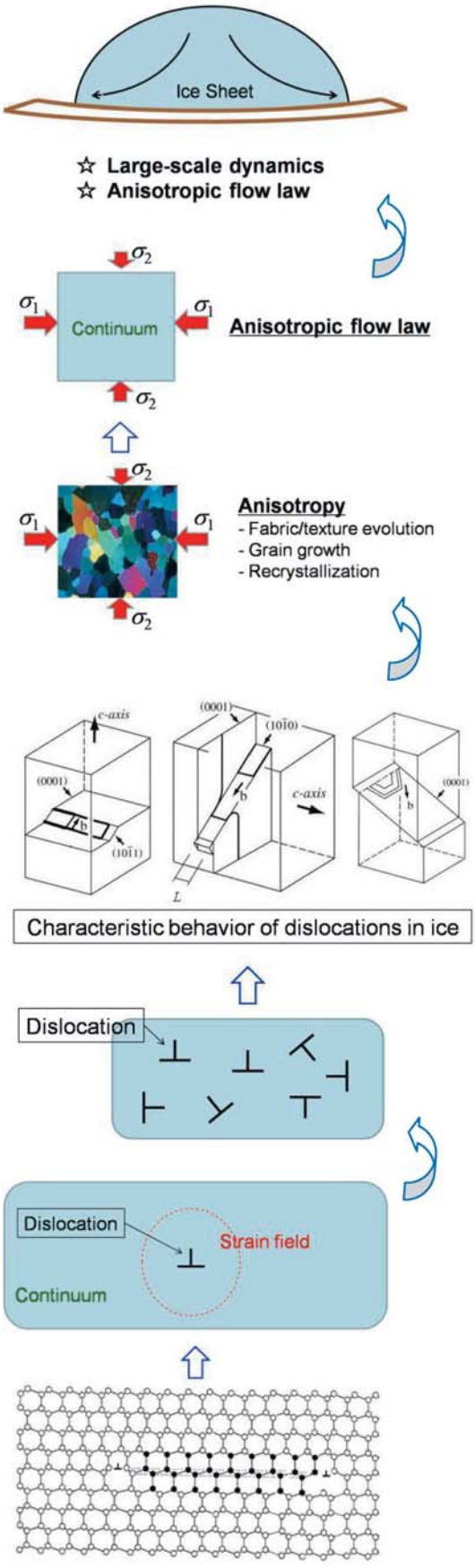

Fig. 23. Structural hierarchy for ice sheet flow modeling.

simulations make it possible to calculate the positions of all molecules during deformation, it is impossible to extend this method to ice sheet flow dynamics. Instead, by introducing the concept of dislocation, the same phenomenon can be explained by describing the behavior of only a few dislocations, as shown in the second step of the hierarchy. As can be seen in this example, we have to develop a new concept or theory to give an essentially simplified picture of a complex phenomenon, in order to jump to a higher hierarchical level. On the other hand, to improve the ice sheet flow model at the top of the hierarchy, we have to take into consideration the processes or mechanisms revealed at lower hierarchical level. Recent developments in anisotropic flow dynamics provides invaluable examples for this purpose [12, 13, 80], although we still have many missing links between the base and the top of the hierarchy sequence seen in Fig. 23.

Future prospects for research into the fundamental aspects and applications of nanoglaciology can be stated as follows.

(1) Atmospheric aerosols in the past

Ice cores can be a unique archive of atmospheric aerosols in the past since water-soluble and insoluble microparticles are present. For reliable reconstructions of past radiative forcing caused by atmospheric aerosols, we must know the concentrations and size distributions of the aerosol particles together with their chemical forms, including the hydration numbers. Such data can be obtained from ice cores as described in this article, paying careful attention to post-depositional alteration of the microparticles.

(2) Application of the Iizuka diagram to deduce new information on paleoclimate and paleoenvironment

As described in section 3, Iizuka *et al.* [7] developed a diagram to help ascertain the major chemical forms that remain stable in ice at particular depths where the principal concentrations of ions are known. This diagram provides a great facility in indicating the major chemical forms of microparticles, or aerosols, without direct observation. Much more reliable analyses for paleo-aerosols are expected through using this scheme, in conjunction with the results of chemical analyses that we already have.

In addition to the application of the Iizuka diagram, depth profiles of water-soluble microparticles are also required to further refine the records. The sublimation method developed by Iizuka will assist in the effective collection of these microparticles.

(3) Application of dislocation mechanisms to anisotropic ice sheet flow models

Ice sheet flow models should include all the physical processes that might affect flow dynamics. As described in section 4, dislocations during movement within the non-basal planes play important roles in generation of the basal dislocations and the stored strain energy. Moreover, the interaction behavior of dislocation and grain boundaries should be taken into consideration for the ice flow law, as discussed by Louchet *et al.* [81] in this volume. It is most challenging to develop ice sheet flow models in which dislocation mechanisms are involved. Although anisotropy is already considered in recently developed flow models [12, 13, 80], it is required to construct the missing links shown in Fig. 23.

(4) Reconsideration of the texture evolution

As described in subsections 3.3 and 4.6, new phases in the texture evolution can be expected if we take into consideration water-soluble microparticles and all of the slip systems including the characteristic behavior of non-basal dislocation. This is important in linking anisotropic flow models with dislocation behavior, and in order to deduce new information on past ice sheets.

(5) Modeling of firn densification processes

As described in subsection 2.4, almost all of the physical processes related to firn densification have been revealed by recent experimental and theoretical studies. A new advanced model is required to assemble all of the firn densification processes. It is necessary to establish more reliable methods for the determination of ice core chronology and to identify new proxy indicators for paleoclimate and paleoenvironment.

(6) Fresh views on radio-echo sounding

As briefly described in section 5, the data obtained by the new methods of radio-echo sounding are invaluable in extending the information obtained from ice core analyses over a wide ice sheet area. In particular, the radio-echo sounding data related to crystal-orientation fabric must be important to improve anisotropic ice sheet flow models.

(7) Reconsideration of high time-resolution records

Since the behaviors of chemical species and gas molecules in ice sheets have been clarified as described in this article, reconsideration is required on reliability and accuracy of various proxies, related to atmospheric and climate changes. It is particularly important to have a complete understanding of the physical/chemical processes in order to establish reliability in the high time-resolution of ice core records [56, 82].

It should be emphasized that both atmospheric air, including greenhouse gasses and aerosols, and ice sheets situated around the north and south poles are most important key players in the global climate system. Ice cores are an archive of invaluable data contributing toward the understanding of the past behavior of both players. This archive has a huge potential in the future advancement of knowledge of the Earth's climate and environment.

Acknowledgements

I thank all the members of the ice core research group in the Institute of Low Temperature Science, Hokkaido University, for their contributions to the studies. I am also grateful to all the participants of the

Dome Fuji project for their invaluable contributions to successful ice coring. Drs. Y. Iizuka, T. Sakaurai, H. Ohno, A. Miyamoto, S. Fujita and R. Greve provided invaluable discussion and comments that significantly helped to improve the manuscript. Dr. T. H. Jacka kindly made valuable suggestions regarding the mechanical properties of ice. I appreciate the FE-SEM photograph assistance of Drs. T. Fukui, K. Tomioka and Y. Iizuka. They helped to take the microparticle photographs shown in Fig. 7. This research was supported by a Grant-in-Aid for Creative Scientific Research (No. 14GS0202) from the Japanese Ministry of Education, Culture, Sports, Science and Technology.

References

[1] T. Ikeda, H. Fukazawa, S. Mae, L. Pepin, P. Duval, B. Champagnon, V. Ya. Lipenkov and T. Hondoh. Extreme fractionation of gases caused by formation of clathrate hydrates in Vostok Antarctic ice. *Geophys. Res. Lett.*, 26(1): 91-94, 1999.

[2] T. Ikeda, A. N. Salamatin, V. Ya. Lipenkov and T. Hondoh. Diffusion of air molecules in polar ice sheets. In T. Hondoh, editor, *Physics of Ice Core Records*, Hokkaido University Press, Sapporo, 393-421, 2000.

[3] A. N. Salamatin, V. Ya. Lipenkov, T. Ikeda-Fukazawa and T. Hondoh. Kinetics of air-hydrate nucleation in polar ice sheets. *J. Cryst. Growth*, 223: 285-305, 2001.

[4] T. Ikeda-Fukazawa, T. Hondoh, T. Fukumura, H. Fukazawa and S. Mae. Variation in N_2/O_2 ratio of occluded air in Dome Fuji Antarctic ice. *J. Geophys. Res.*, 106(D16): 17799-17810, 2001.

[5] H. Ohno, M. Igarashi and T. Hondoh. Salt inclusions in polar ice core: Location and chemical form of water-soluble impurities. *Earth and Planet. Sci. let.*, 232: 171-178, 2005.

[6] H. Ohno, M. Igarashi and T. Hondoh. Characteristics of salt inclusions in polar ice from Dome Fuji, East Antarctica. *Geophys. Res. Lett.*, 33(8): Article No. L08501, 1-5, 2006.

[7] Y. Iizuka, S. Horikawa, T. Sakurai, S. Johnson, D. Dahl-Jensen, J. P. Steffensen and T. Hondoh. A relationship between ion balance and the chemical compounds of salt inclusions found in the Greenland Ice Core Project and Dome Fuji ice cores. *J. Geophys. Res. (Atmosphere)*, 113(D7): Article No. D07303, 2008.

[8] Y. Iizuka, T. Miyake, M. Hirabayashi, T. Suzuki, S. Matoba, H. Motoyama, Y. Fujii, and T. Hondoh. Constituent elements of insoluble and nonvolatile particles during the Last Glacial Maximum of the Dome Fuji ice core. *J. Glaciol.*, 55(191): 552-562, 2009.

[9] Y. Iizuka, T. Hondoh, and Y. Fuji. Na_2SO_4 and $MgSO_4$ salts during Holocene period in a Dome Fuji ice core derived by high depth-resolution analysis. *J. Glaciol.*, 52(176): 58-64, 2006.

[10] O. Gagliardini and J. Meyssonnier. Simulation of anisotropic ice flow and fabric evolution along the GRIP-GISP2 flow line (central Greenland). *Ann. Glaciol.*, (30): 217–223, 2000.

[11] H. Seddik, R. Greve, T. Zwinger and L. Placidi. A full-Stokes ice flow model for the vicinity of Dome Fuji, Antarctica, with induced anisotropy and fabric evolution. *The Cryosphere Discuss.*, 3(1): 1-31, 2009.

[12] R. Greve, L. Placidi and H. Seddik. A continuum-mechanical model for the flow of anisotropic polar ice. In T. Hondoh, editor, *Physics of Ice Core Records II*, Supplement Issue of Low Temperature Science, Vol. 68: 2009 (this volume).

[13] O. Gagliardini, F. Gillet-Chaulet, and M. Montagnat. A Review of Anisotropic Polar Ice Models: from crystal to ice-sheet flow models. In T. Hondoh, editor, *Physics of Ice Core Records II*, Supplement Issue of Low Temperature Science, Vol. 68: 2009 (this volume).

[14] H. Ohno, V. Y. Lipenkov and T. Hondoh. Air bubble to clathrate hydrate formation in polar ice sheets: a reconsideration based on the new data from Dome Fuji ice core. *Geophys. Res. Lett.*, 31, L21401, doi: 10.1029/2004GL021151, 2004.

[15] T. Sakurai. *Studies on phase equilibrium states and special distributions of water-soluble microparticles preserved in polar ice sheets.* Doctoral Thesis, Graduate School of Environmental Science, Hokkaido University, Sapporo, Japan, (Thesis in preparation).

[16] A. W. Rempel, J. S. Wettlaufer and E. D. Waddington, Anomalous diffusion of multiple impurity species: predicted implications for the ice core climate records. *J. Geophys. Res.* 107, B122330, doi:10.1029/2002JB001857, 2002.

[17] Y. Iizuka, H. Ohno, T. Sakurai, S. Horikawa and T. Hondoh. Chemical compounds of water-soluble impurities in Dome Fuji ice core. *Physics of Ice Core Records II*, Supplement Issue of Low Temperature Science, Vol. 68: 2009 (this volume).

[18] N. H. Fletcher. *The Chemical Physics of Ice*. Cambridge Univ. Press, Cambridge: 271 pp., 1970.

[19] V. F. Petrenko and R. W. Whitworth. *Physics of Ice.* Oxford Univ. Press, New York: 373 pp., 1999.

[20] T. Ikeda-Fukazawa and T. Hondoh. Behavior of air molecules in polar ice sheets. *Memoirs of National Institute of Polar Research*, Special Issue (57): 178-186, 2003.

[21] T. Ikeda-Fukazawa, S. Horikawa, T. Hondoh and K. Kawamura. Molecular dynamics studies of molecular diffusion in ice I_h. *J. Chem. Phys.*, 117 (8): 3886-3896, 2002.

[22] A. N. Salamatin, T. Hondoh, T. Uchida and V. Ya .Lipenkov. Post-nucleation conversion of an air bubble to clathrate air-hydrate crystal in ice. *J. Cryst. Growth*, 193: 197-218, 1998.

[23] A. N. Salamatin, V. Ya. Lipenkov and T. Hondoh. Air-hydrate crystal growth in polar ice. *J. Cryst. Growth*, 257: 412-426, 2003.

[24] T. Hondoh. Clathrate hydrates in polar ice sheets. *Proc. 2nd Int. Conf. Natural Gas Hydrates*: 131-138, 1996.

[25] H. Ohno, V. Ya. Lipenkov and T. Hondoh. Formation of air clathrate hydrates in polar ice sheets: heterogeneous nucleation induced by micro-inclusions. (Paper in preparation).

[26] T. Hondoh. Growth process of clathrate-hydrate crystals in deep ice sheet (in Japanese), *Nihon Kessyou Seichou Gakkai Shi*, 16: 149-161, 1989.

[27] W. Shimada, and T. Hondoh. In situ observation of the transformation from air bubbles to air clathrate hydrate crystals using a Mizuho ice core. *J. Cryst. Growth*, 265: 309-317. 2004.

[28] T. Uchida, S. Mae, T. Hondoh, P. Duval and V. YA. Lipenkov. Measurements of surface energy of air-hydrate crystals in Vostok ice core, Antarctica. *Proc. NIPR Symp. Polar Meteorol. Glaciol.*, 7: 1-6, 1993.

[29] H. Shoji and C. C. Langway. Air hydrate inclusions in fresh ice core. *Nature* 298 (5874): 548-550, 1982.

[30] S. Kipfstuhl, F. Pauer, W. F. Kuhs and H. Shoji. Air bubbles and clathrate hydrates in the transition zone of the NGRIP deep ice core. *Geophys. Res. Lett.*, 28 (4): 591-594, 2001.

[31] A. Miyamoto, T. Saito and T. Hondoh. Visual observation of volume relaxation under different storage temperature in the Dome Fuji ice core, Antarctica. In T. Hondoh, editor, *Physics of Ice Core Records II*, Supplement Issue of Low Temperature Science, Vol. 68: 2009 (this volume).

[32] T. Uchida and T. Hondoh. Laboratory studies on air-hydrate crystals. In T. Hondoh, editor, *Physics of Ice Core Records*. Hokkaido University Press, Sapporo: 423-457, 2000.

[33] T. Ikeda-Fukazawa, K. Fukumizu, K. Kawamura, S. Aoki, T. Nakazawa and T. Hondoh. Effects of molecular diffusion on trapped gas composition in polar ice cores. *Earth Planet. Sci. Lett.*, 229: 183-192, 2005.

[34] B. Bereiter, J. Schwander, D. Luthi and T. F. Stocker. Change in CO_2 concentration and O_2/N_2 ratio in ice cores due to molecular diffusion. *Geophys. Res. Lett.,* 36: Article No. L05703, 1-5, 2009.

[35] K. Goto, T. Hondoh, and A. Higashi. *Jpn. J. Appl. Phys.*, 25(3): 351-357, 1986.

[36] T. Hondoh, R. Hoshi, A. Goto and H. Yamakami. A new method using synchrotron-radiation topography for determining point-defect diffusivity under hydrostatic pressure. *Philos. Mag. Lett.*, 63(1): 1-5, 1991.

[37] A. Fukuda, T. Hondoh and A. Higashi. Dislocation mechanisms of plastic deformation of ice. *J. Phys.*, 48, C1: 163-171, 1987.

[38] T. Hondoh. Nature and behavior of dislocations in ice. In T. Hondoh, editor, *Physics of Ice Core Records*. Hokkaido University Press, Sapporo, 3-24, 2000.

[39] T. Hondoh, T. Itoh and A. Higashi. Formation of stacking faults in pure ice single crystals by cooling. *Jpn. J. Appl. Phys.*, 20(10): L737-740, 1981.

[40] T. Hondoh, T. Itoh, S. Amakai K. Goto and A. Higashi. Formation and annihilation of stacking faults in pure ice. *J. Phys. Chem.*, 87(21): 4040-4044, 1983.

[41] A. Higashi, A. Fukuda, M. Oguro, T. Hondoh, H. Shoji and K. Azuma. *Lattice Defects in Ice Crystals*. Hokkaido Univ. Press, 156 pp., 1988.

[42] T. Hondoh. Synchrotron-radiation topographic studies on dynamic behavior of lattice defects: Dislocation climb and point-defect diffusivity. *Radiation Effects and Defects in Solids*, 124: 139-145, 1992.

[43] A. A. Ekaykin and V. Ya. Lipenkov. Formation of the ice core isotopic composition. In T. Hondoh, editor, *Physics of Ice Core Records II*, Supplement Issue of Low Temperature Science, Vol. 68: 2009 (this volume).

[44] A. Landais, E. Barkan, F. Vimeux, V. Masson-Delmotte and B. Luz. Combined analysis of water stable isotopes ($H_2{}^{16}O$, $H_2{}^{17}O$, $H_2{}^{18}O$, $HD^{16}O$) in ice cores. In T. Hondoh, editor, *Physics of Ice Core Records II*, Supplement Issue of Low Temperature Science, Vol. 68: 2009 (this volume).

[45] K. Weiler, J. Schwander, M. Leuenberger, T. Blunier, R. Mulvaney, P. S. Anderson, R. Salmon and W. T. Sturges. Seasonal variations of isotope ratios and CO_2 concentrations in firn air. In T. Hondoh, editor, *Physics of Ice Core Records II*, Supplement Issue of Low Temperature Science, Vol. 68: 2009 (this volume).

[46] A. N. Salamatin, V. Ya. Lipenkov, J. M. Barnola, A. Hori, P. Duval and T. Hondoh. Snow/firn densification in polar ice sheets. In T. Hondoh, editor, *Physics of Ice Core Records II*, Supplement Issue of Low Temperature Science, Vol. 68: 2009 (this volume).

[47] S. Fujita, J. Okuyama, A. Hori, and T. Hondoh. Metamorphism of stratified firn at Dome Fuji, Antarctica: A mechanism for local insolation modulation of gas transport conditions during bubble close off. *J. Geophys. Res. (Earth Surface)*, 114: Article No. F03023, 2009.

[48] M. L. Bender. Orbital tuning chronology for the Vostok climate record supported by trapped gas composition. *Earth Planet. Sci. Lett.*, 204(1-2): 274-289, 2002.

[49] K. Kawamura, F. Parrenin, L. Lisiecki, R. Uemura, F. Vimeux, J. P. Severinghaus, M. A. Hutterli, T. Nakazawa, S. Aoki, J. Jouzel, M. E. Raymo, K. Matsumoto, H. Nakata, H. Motoyama, S. Fujita, K. Azuma, Y. Fujii and O. Watanabe. Northern Hemisphere forcing of climatic cycles over the past 360,000 years implied by accurately dated Antarctic ice cores. *Nature*, *448*(7156): 912-916, 2007.

[50] D. Raynaud, V. Ya. Lipenkov, B. Lemieux-Dudon, P. Duval, M.-F. Loutre and N. Lhomme. The local insolation signature of air content in Antarctic ice. A new step toward an absolute dating of ice records, *Earth Planet. Sci. Lett.*, *261*(3-4): 337-349, 2007.

[51] B. Lemieux-Dudon, F. Parrenin and E. Blayo. A probabilistic method to construct an optimal ice chronology for ice cores. In T. Hondoh, editor, *Physics of Ice Core Records II*, Supplement Issue of Low Temperature Science, Vol. 68: 2009 (this volume).

[52] J. P. Severinghaus, and M. O. Battle. Fractionation of gases in polar ice during bubble close-off: New constraints from firn air Ne, Kr and Xe observations. *Earth Planet. Sci. Lett.*, *244*(1-2): 474-500, 2006.

[53] K. Kawamura, T. Nakazawa, S. Aoki, Y. Fujii, O. Watanabe and J. Severinghaus. Close resemblance between local summer insolation, O_2/N_2 and total air content from the Dome Fuji ice core, Antarctica. Paper presented at Eos Trans. AGU, 85(47), Fall Meet. Suppl., Abstract C33C-0356. 2004.

[54] M. A. Hutterli, M. Schneebeli, J. Freitag, J. Kipfstuhl and R. Röthlisberger. Impact of local insolation on Snow metamorphism and ice core records. In T. Hondoh, editor, *Physics of Ice Core Records II*, Supplement Issue of Low Temperature Science, Vol. 68: 2009 (this volume).

[55] Y. Iizuka, M. Takata, T. Hondoh and Y. Fuji. High-time-resolution profiles of soluble ions in the last glacial period of a Dome Fuji (Antarctica) deep ice core. *Ann. Glaciol.*, 39: 452-456, 2005.

[56] Y. Iizuka, T. Hondoh, Y. Fujii. Antarctic sea ice extent during the Holocene reconstructed from inland ice core evidence. *J. Geophys. Res. (Atmosphere)*, 113(D15): Article No. D15114, 2008.

[57] F. E. Genceli, , Horikawa, S., Iizuka, Y., Sakurai, T., Hondoh, T., Kawamura, T. and Witkamp, G-J, Meridianiite detected in ice, *J. Glaciol.*, 55(189): 117-122, 2009.

[58] T. Sakurai, Y. Iizuka, S. Horikawa, S. Johnsen, D. Dahl-Jensen, J.P. Steffensen, and T. Hondoh, Direct observation of salts as micro-inclusions in the Greenland GRIP ice core. *J. Glaciol.*, 55(193): 777-783, 2009.

[59] J. C. Moore and A. Grinsted. Ion fractionation and percolation in ice cores with seasonal melting. In T. Hondoh, editor, *Physics of Ice Core Records II*, Supplement Issue of Low Temperature Science, Vol. 68: 2009 (this volume).

[60] N. Azuma, Y. Wang, Y. Yoshida, H. Narita, T. Hondoh, H. Shoji and O. Watanabe. Crystallographic analysis of the Dome Fuji ice core. In T. Hondoh, editor, *Physics of Ice Core Records*. Hokkaido University Press, Sapporo: 83-102, 2000.

[61] G. Durand, J. Weiss, V. Lipenkov, J. M. Barnola, G. Krinner, F. Parrenin, B. Delmonte, C. Ritz, P. Duval, R. Rothlisberger and M. Bigler. Effect of impurities on grain growth in cold ice sheets. *J. Geophys. Res.*, 111, F01015: 1-18, 2006.

[62] G. Durand, A. Svensson, A. Persson, O.

Gagliardini, F. Gillet-Chaulet, J. Sjolte, M. Montagnat and D. Dahl-Jensen. Evolution of the texture along the EPICA Dome C ice core. In T. Hondoh, editor, *Physics of Ice Core Records II*, Supplement Issue of Low Temperature Science, Vol. 68: 2009 (this volume).

[63] R. B. Alley, J. H. Perepezko and C. R. Bentley. Grain growth in polar ice: I. Theory. J. Glaciol., 32 (112): 415-424, 1986.

[64] J. P. Hirth and J. Lothe. *Theory of Dislocations*. McGraw-Hill, New York etc., 780 pp., 1968.

[65] M. Schulson and P. Duval, *Creep and Fracture of Ice*. Cambridge University Press, Cambridge etc., 401 pp., 2009.

[66] T. Hondoh, H. Iwamatsu and S. Mae. Dislocation mobility for nonbasal glide in ice measured by in situ X-ray topography. *Philos. Mag.*, A62(1): 89-102, 1990.

[67] T. H. Jacka and J. Li. Flow rates and crystal orientation fabrics in compression of polycrystalline ice at low temperatures and stresses, In T. Hondoh, editor, *Physics of Ice Core Records*. Hokkaido University Press, Sapporo, 83-102, 2000.

[68] I. Weikusat, S. Kipfstuhl, N. Azuma, S. H. Faria and A. Miyamoto. Deformation microstructures in an Antarctic ice core (EDML) and in experimentally deformed artificial ice. In T. Hondoh, editor, *Physics of Ice Core Records II*, Supplement Issue of Low Temperature Science, Vol. 68: 2009 (this volume).

[69] M. Montagnat, G. Durand and P. Duval. Recrystallization processes in granular ice. In T. Hondoh, editor, *Physics of Ice Core Records II*, Supplement Issue of Low Temperature Science, Vol. 68: 2009 (this volume).

[70] A. Svensson, G. Durand, J. Mathiesen, A. Persson, D. Dahl-Jensen. Texture of the Upper 1000 m in the GRIP and North GRIP Ice Cores. In T. Hondoh, editor, *Physics of Ice Core Records II*, Supplement Issue of Low Temperature Science, Vol. 68: 2009 (this volume).

[71] S. Donoghue and T. H. Jacka. The stress pattern within the Law Dome summit to Cape Folger ice flow line, inferred from measurements of crystal fabric. In T. Hondoh, editor, *Physics of Ice Core Records II*, Supplement Issue of Low Temperature Science, Vol. 68: 2009 (this volume).

[72] T. H. Jacka and Li Jun. The steady-state crystal size of deforming ice. *Ann. Glaciol.* 20: 13-18, 1994.

[73] C. Allen. A brief history of radio-echo sounding of ice. *Earthzine*, Sept. 26th, 2008. (http://www.earthzine.org/2008/09/26/a-brief-history-of-radio-echo-sounding-of-ice/)

[74] S. Fujita, K. Matsuoka, H. Maeno and T. Furukawa. Scattering of VHF radio waves from within an ice sheet containing the vertical-girdle-type ice fabric and anisotropic reflection boundaries. *Ann. Glaciol.*, 37: 305-316, 2003.

[75] K. Matsuoka, S. Uratsuka, S. Fujita, and F. Nishio. Ice-flow induced scattering zone within the Antarctic ice sheet revealed by high-frequency airborne radar, *J. Glaciol.*, 50(170): 382–388, 2004.

[76] S. Fujita, H. Maeno and K. Matsuoka. Radio-wave depolarization and scattering within ice sheets: a matrix-based model to link radar and ice-core measurements and its application. *J. Glaciol.*, 52(178): 407-424, 2006.

[77] S. H. Faria. The multidisciplinary ice core. In T. Hondoh, editor, *Physics of Ice Core Records II*, Supplement Issue of Low Temperature Science, Vol. 68: 2009 (this volume).

[78] S. H. Faria, S. Kipfstuhl, N. Azuma, J. Freitag, I. Hamann, M. M. Murshed and W. F. Kuhs. The multiscale structure of Antarctica. Part I: Inland ice. In T. Hondoh, editor, *Physics of Ice Core Records II*, Supplement Issue of Low Temperature Science, Vol. 68: 2009 (this volume).

[79] N. Kirchner and S. H. Faria. The multiscale structure of Antarctica. Part II: Ice shelves. In T. Hondoh, editor, *Physics of Ice Core Records II*, Supplement Issue of Low Temperature Science, Vol. 68: 2009 (this volume).

[80] R. Greve and H. Blatter. *Dynamics of Ice Sheets and Glaciers.* Springer-Verlag Berlin, Heidelberg 2009.

[81] F. Louchet, P. Duval, M. Montagnat and J. Weiss. Are self-organised critical dislocation dynamics relevant to ice sheet flow? In T. Hondoh, editor, *Physics of Ice Core Records II.*, Supplement Issue of Low Temperature Science, Vo. 68: 2009 (this volume).

[82] C. Huber and M. Leuenberger. Measurements of isotope and elemental ratios of air from polar ice with a new on-line extraction method. *Geochem. Geophys. Geosyst.*, 5, Q10002, doi: 10.1029/2004GC000766, 2004.